NASA-CR-194412

IN-25

[illegible]

186236

64 P

Final Technical Report on:

IMMISCIBLE PHASE INCORPORATION DURING DIRECTIONAL SOLIDIFICATION OF HYPERMONOTECTICS

Submitted by

J. Barry Andrews and Roger A. Merrick
Department of Materials Science and Engineering
University of Alabama at Birmingham
Birmingham, Alabama 35294-4461

for

NASA Research Grant NAG8-768
George C. Marshall Space Flight Center
Marshall Space Flight Center, Alabama 35812

August, 1993

(NASA-CR-194412) IMMISCIBLE PHASE INCORPORATION DURING DIRECTIONAL SOLIDIFICATION OF HYPERMONOTECTICS Final Report (Alabama Univ.) 64 p

N94-14480

Unclas

G3/25 0186236

ABSTRACT

In this study, solidification processes in immiscible samples were investigated by directly observing the events taking place at the solid-liquid interface during directional solidification. Visualization of these events was made possible through the use of a transparent metal analogue system and a temperature gradient stage assembly fitted to an optical microscope.

The immiscible transparent analogue system utilized in this study was the succinonitrile-glycerol system. This system has been shown to exhibit the same morphological transitions as observed in metallic alloys of monotectic composition. Both monotectic and hypermonotectic composition samples were directionally solidified in order to gain an improved understanding of the manner in which the excess hypermonotectic liquid is incorporated into the solidifying structure. The processing conditions utilized in this study prevented sedimentation of the excess hypermonotectic liquid by directionally solidifying the samples in very thin (13μm), horizontally oriented cells.

High thermal gradient to growth rate ratios (G/R) were used in an effort to prevent constitutional supercooling and the subsequent formation of L_2 droplets in advance of the solidification front during the growth of fibrous composite structures. Results demonstrated that hypermonotectic composites could be produced in samples up to two weight percent off of the monotectic composition by using a G/R ratio greater than or equal to $4.6\text{x}10^4$ °C·s/mm^2 to avoid constitutional supercooling. For hypermonotectic samples processed with G/R ratios below $4.6\text{x}10^4$ °C·s/mm^2, constitutional supercooling occurred and resulted in slight interfacial instability. For these samples, two methods of incorporation of the hypermonotectic liquid were observed and are reported here.

The correlation between the phase spacing, λ, and the growth rate, R, was examined and was found to obey a relationship generally associated with a diffusion controlled coupled growth process. For samples with compositions ranging from the monotectic composition up to 2% off of the monotectic composition, data indicated that the square of the phase spacing (λ) varied linearly with the inverse of the growth rate (R).

TABLE OF CONTENTS

TABLE OF CONTENTS (Continued)

APPENDIXES

INTRODUCTION

Many unusual and useful characteristics have been predicted for immiscible alloys. A wide variety of potential applications was noted in a report by Reger[1] which covered over 300 immiscible metal alloy systems. Applications included bearing materials, high performance electrical contact materials, breeder reactor fuels, nuclear reactor control rods, dispersion-strengthened alloys, high-coercivity permanent magnets, and composite superconducting materials. When one considers all of the possible uses for immiscible alloys, the interest in developing a better scientific understanding of these materials becomes apparent.

Monotectic systems are the most common example of alloys which exhibit immiscible liquid behavior. Monotectic alloys contain a distinctive range of compositions and temperatures over which two compositionally different liquids coexist. This region has been termed the miscibility gap. A schematic drawing of a monotectic phase diagram is shown in Figure 1(a), where C_m denotes the monotectic composition and T_m the monotectic temperature.

The monotectic reaction,

$$L_1 \rightleftharpoons S_1 + L_2, \qquad [1]$$

involves a single-phase liquid transforming to a single-phase solid and a single-phase liquid of a different composition upon cooling. An extensive variety of microstructures can be obtained during the solidification of alloys of monotectic and near-monotectic compositions.[2,3] The morphology of the structure obtained during directional solidification is dependent on many factors including composition, growth rate, the thermal gradient used during processing, and the height of the miscibility gap.[2,3]

In order to optimize the properties of immiscible alloys, it is desirable to produce a microstructure which contains a high volume fraction of the L_2 phase as either aligned fibers or as a fine dispersion, depending upon the application. A significant amount of work has been carried out utilizing low-g conditions to obtain finely dispersed microstructures in monotectic systems.[4-14] However, the current study is focused on producing an aligned fibrous structure containing a high volume fraction of the L_2 phase.

Aligned structures have been obtained in alloys of monotectic composition in the past[2-4,15-25] but in general, these structures contain less than 10% of the L_2 phase by

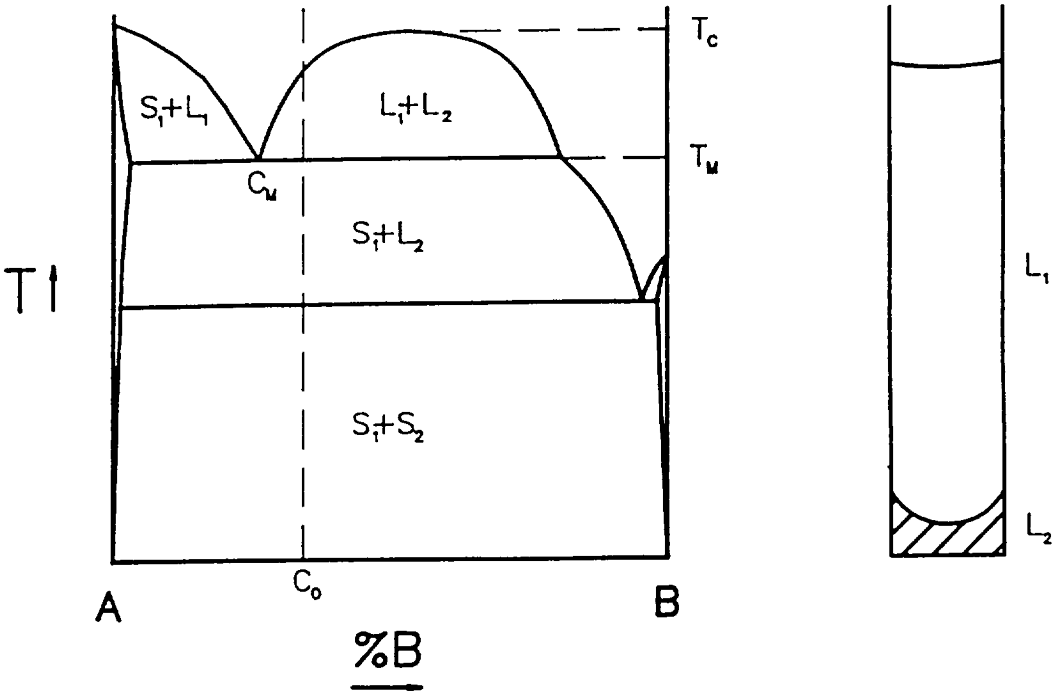

Figure 1. Schematic diagrams representing (a) a binary monotectic phase diagram and (b) the result of cooling a hypermonotectic alloy into the miscibility gap under normal gravity conditions.

volume. The volume fraction of L_2 can be increased through the use of alloys of hypermonotectic composition. However, the use of these alloys often leads to difficulties during processing.

The solidification path of a hypermonotectic alloy, such as C_o in Figure 1(a), includes an event not found in alloys of monotectic composition. The first event to occur upon cooling a homogeneous hypermonotectic liquid is separation of the single-phase liquid into two compositionally dissimilar liquids, L_1 and L_2, when the alloy is cooled through the miscibility gap. In most known systems, the densities of L_1 and L_2 are considerably different, with L_2 being the denser of the two phases. As a result, sedimentation of the L_2 phase occurs, as shown schematically in Figure 1(b). As a result of the separation and sedimentation of the L_2, the remaining liquid is of approximately monotectic composition.

The sedimentation of the dense L_2 phase upon cooling, which has been noted by other investigators[3,16-18,26-28], is one of the major barriers to producing aligned microstructures containing a high volume fraction of the immiscible phase. Some work has been conducted involving the directional solidification of hypermonotectic alloys[3-5,16-18,20,22-24,27-30], but because of the sedimentation problem there has only been a limited amount of success.[16-18,27,29]

In addition to the sedimentation problem, many other factors are known to have an influence on the type of structures obtained during directional solidification of immiscible alloys. Some of these factors include the contact angles between phases at the growth front[19], the miscibility gap height[31], the ratio of the liquidus slopes, the volume fraction of the fibrous phase, and the degree of undercooling at the solidification front during the coupled growth process.[32] These factors and others must be considered when attempting to produce a desirable microstructure in immiscible systems.

The research reported in this study took advantage of the characteristics of transparent analogue systems to directly observe the solidification reactions taking place at the growth front. This approach permitted a visual examination of how particular microstructures were formed during directional solidification of alloys of monotectic and hypermonotectic composition. Other investigators have used a similar approach to expand the knowledge of solidification processes in many other systems as well.[21,33-40]

BACKGROUND

Over the years, many significant contributions have been made to understanding the solidification events which occur during processing alloys of monotectic composition. The effects of composition, growth rate, thermal gradient, interfacial energies, disjoining pressure, height of the miscibility gap, undercooling, and many other factors on the resulting microstructures in monotectic alloys have been considered. A progression of the theories and models covering solidification of monotectics will be discussed in the following sections.

Solidification Theory in Monotectic Alloys

Interfacial Energy Effects

In 1965, Chadwick[19] suggested that for an alloy of monotectic composition, the interfacial energies between the reacting phases would be the controlling factors influencing the morphology of the structure obtained during directional solidification. Chadwick[19] stated that in order to produce an aligned fibrous structure in a monotectic alloy, equilibrium contact must occur at the interface between the reacting phases, S_1, L_1, and L_2. This is shown schematically in Figure 2(a). This equilibrium contact between phases was only expected to occur when the interfacial energies were such that $\sigma_{S_1L_2}<\sigma_{S_1L_1}+\sigma_{L_1L_2}$.

In 1979, Cahn[31] established a relationship between the interfacial energies of the phases and temperature in a monotectic system. His analysis was based on the observation that the two immiscible liquids, L_1 and L_2, become compositionally identical at the critical temperature, T_c. Because the liquids become compositionally identical at the critical temperature, T_c, the interfacial energy between the L_1 and L_2 phases, $\sigma_{L_1L_2}$, must go to zero. As the temperature falls below T_c, $\sigma_{L_1L_2}$ increases due to the increasing difference between the compositions of the two immiscible liquids.

This variation in interfacial energy with temperature led to the observation that equlibrium contact between the three phases and the formation of a regular aligned structure was expected to occur in systems with a high miscibility gap. Low miscibility gap systems were expected to form an irregular microstructure.

Structural Transitions

In addition to this surface energy criteria, it has been shown that for metallic alloys of monotectic composition, even if the interfacial energies are correct for composite growth, the type of microstructure obtained can vary with growth rate and thermal gradient.[2,3,15,16,18] At low growth rates and high thermal gradients, a well-aligned arrangement of S_2 fibers can be produced in the S_1 matrix.[43]

However, this fibrous structure is not formed at growth rates much above 5 μm/s.[3,15,16,18] Some investigators report that at higher growth rates or lower thermal gradients, a regular array of doubly aligned spheres is often formed.[2,3,15,21,33] These spheres are aligned both parallel and perpendicular to the growth direction. However, recent communication[44] raises questions as to whether or not this change from fibers to doubly aligned spheres is actually a microstructural transition.

At even higher growth rates or lower thermal gradients, a randomly dispersed structure replaces the arrayed structure.[2,3,15,18,21] These structures apparently arise from a fine interwoven network of L_2 fibers that grows with little directionality. These fibers appear to ripen rapidly into spherical droplets and coarsen.[15] The result is a dispersed structure.

These changes in morphology with growth rate have been seen by many investigators in alloys of monotectic composition.[2,3,15,16,18,21,33] In addition to these microstructural transitions, the inter-phase spacing has also been observed to vary with growth rate in monotectic systems.[2,16,25,32,33]

Relationship between growth rate and inter-phase spacing

In 1966, Jackson and Hunt[42] developed a relationship between the phase spacing, λ, (see Figure 2) and solidification rate, R, which stated that for growth of lamellar and fibrous structures in eutectic systems

$$\lambda^2 R = constant. \qquad [2]$$

A rigorous mathematical approach was used by Jackson and Hunt[42] to develop this λ^2R relationship. Their analysis considered many variables including alloy composition, diffusivity in the liquid, melting point of the alloy, heat of fusion per unit volume of the appropriate phases, and specific surface free energies of the interfaces. The resulting mathematical relationship (Eq. 2) was found to be in agreement with experimental results for eutectic systems.[42]

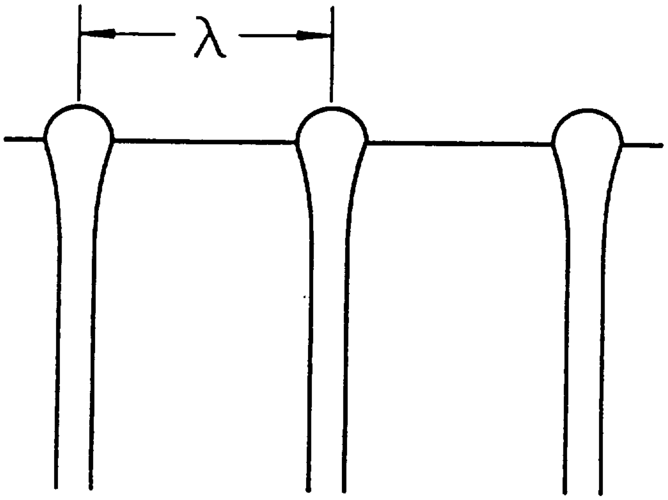

Figure 2. Schematic diagram illustrating the measurement of the phase spacing, λ, for fibrous growth.

Based on similarities between fibrous growth in eutectic and monotectic systems, Livingston and Cline[25] applied the eutectic model to research involving the immiscible Cu-Pb system. The λ^2R relationship was found to be constant, but the value of the constant obtained experimentally by Livingston and Cline[25] was approximately two orders of magnitude greater than that predicted by the model. This discrepancy in the calculated and experimental value of the constant may be related to the system which was studied.

The Cu-Pb system is a wetting (low-dome) system that produces an irregular fibrous morphology by a continuous engulfment process. Other researchers[33] have reported that low-dome systems produce much coarser microstructures than the aligned fibrous morphologies produced through the coupled growth process in high-dome systems. In these investigations, the coarser microstructures resulted in phase spacings that were up to one order of magnitude larger for wetting systems than those obtained for systems which exhibited equilibrium contact between phases.

Livingston and Cline[25] noted that some of the assumptions for the eutectic growth model did not fully represent actual events that occurred during monotectic growth. These researchers reported that the eutectic model ignored diffusion behind the advancing interface because the products of the eutectic reaction were both solid phases. However, the fibrous phase formed during the monotectic reaction is in the liquid state and therefore, diffusion should be a more important factor. As a result, the diffusion process at the interface may be disrupted by mass flow along the axis of the rods during solidification. For these reasons, Livingston and Cline[25] felt that Jackson and Hunt's[42] model did not accurately describe the rod growth process in monotectic alloys.

Another possible problem which was not discussed by Livingston and Cline[25] was Marangoni or thermocapillary convection caused by a variation in surface tension with temperature at the L_1-L_2 interface.[45] The interfacial energy between phases is usually higher at low temperatures (i.e. the S_1-L_1-L_2 triple point) than at higher temperatures (i.e. the fiber tips). If the tips of the L_2 fibers protrude into the L_1 liquid, a variation in the interfacial energy along the L_1L_2 interface due to the applied thermal gradient could create small Marangoni-driven flows on each side of the protruding fiber tips, as shown in Figure 3. As a result, these flows could effect the diffusion process at the growth front.

Grugel, Lagrasso, and Hellawell[33] also carried out an extensive study of the microstructures and phase spacings obtained in monotectic systems. Their study involved the use of both metallic and transparent analogue immiscible systems. The λ^2R relationship (Eq. 2) was found to hold true for monotectic alloys that formed well-aligned fibers (high-dome) and for monotectic alloys that formed irregularly-shaped fibers (low-dome). However, the monotectics that formed irregularly-shaped fibers produced coarser microstructures and yielded a larger constant, as discussed previously.

Considerable work[2,16,25,32,33,34,42,46] has been carried out investigating the linear dependence of the λ^2R relationship in monotectic systems. It should be of great interest to determine if the same relationship holds true for immiscible alloys in the hypermonotectic composition range.

Steady State Growth in Hypermonotectic Alloys

It has been known for some time that eutectic-like composite structures with a higher volume fraction of the pro-eutectic phase than obtainable in alloys of eutectic composition can be produced through directional solidification of off-eutectic composition alloys.[46,48]

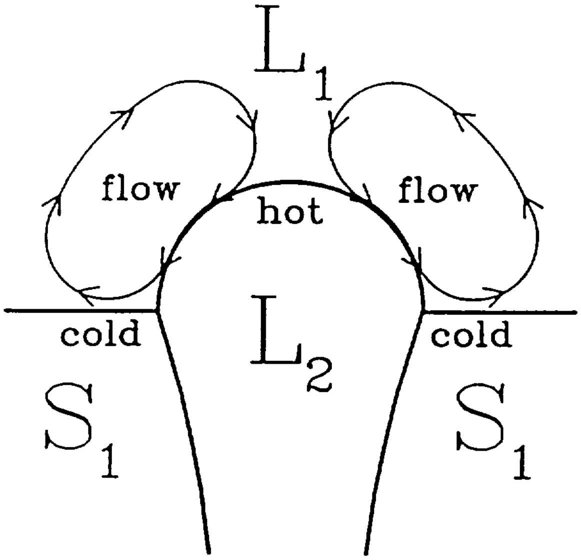

Figure 3. Schematic diagram of possible flows driven by Marangoni type convection at the growth front.

Theoretically, it should also be possible to produce high-volume-fraction, composite structures in hypermonotectic alloys. However, at least two major problems exist in producing these composite structures in alloys of hypermonotectic composition. These problems are related to interfacial and convective instabilities.

Interface Stability

A factor which has often been overlooked when directionally solidifying alloys of off-monotectic composition is that of interface stability. Solidification theory[49] implies that during directional solidification of a hypermonotectic alloy of composition C_o (see Figure 4(a)), a solute depleted boundary layer will form in advance of the growth front. After steady state growth conditions are stabilized, the average composition in the liquid at the growth front is expected to be very close to the monotectic composition, C_m. For a given growth rate, R_1, as the distance from the interface increases, the composition of the liquid in the solute depleted boundary layer should increase exponentially to C_o, the overall alloy composition. This

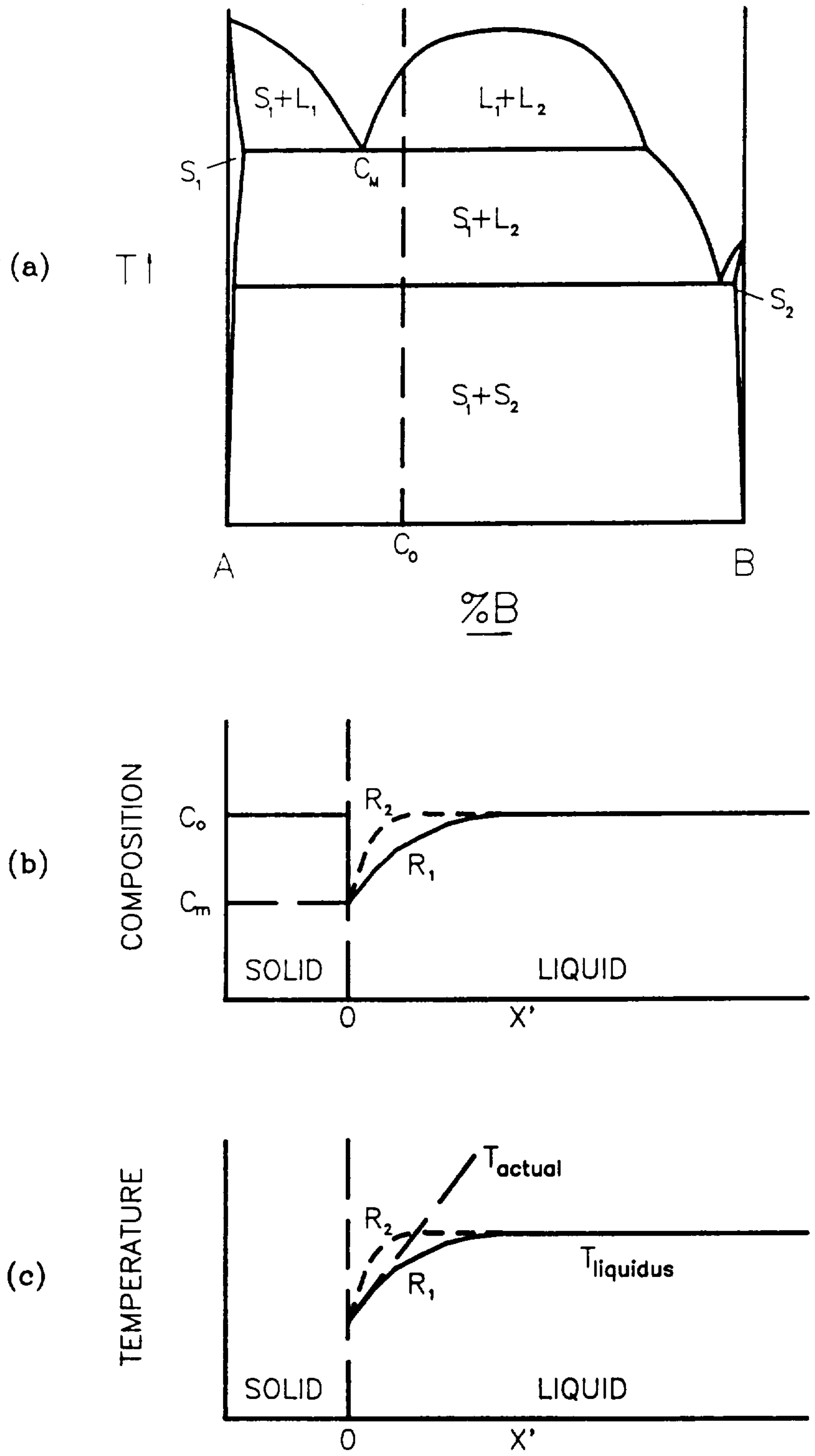

Figure 4. Schematics of (a) monotectic phase diagram; (b) composition profiles for the boundary layer where $R_2 > R_1$; (c) gradient in equilibrium liquidus temperature in the boundary layer.

compositional variation is shown schematically in Figure 4(b). This variation in composition in the solute boundary layer creates a variation in the equilibrium liquidus temperature with distance which can be determined from the phase diagram and is shown schematically in Figure 4(c).

If the thermal gradient imposed upon the sample causes the temperature of the liquid in the boundary layer to drop into the $L_1 + L_2$ region, the primary L_2 phase is expected to form as droplets in advance of the solidification front. This phenomenon is known as "constitutional supercooling" and is well-known in the crystal growth area and in the steady state growth of polyphase alloys.

The equation establishing the conditions for interface stability in single-phase alloys which was originally given by Tiller et al.[50] can be easily modified for coupled growth in polyphase systems.[49] For monotectics, the equation for interface stability would be

$$\frac{G_L}{R} > \frac{m_L\ (C_o - C_m)}{D_L}, \tag{3}$$

where the terms and their units are defined in Table I. The characteristic length, δ, of the solute depleted boundary layer that forms in advance of the solidification front is given by the relationship

$$\delta \propto \frac{D_L}{R}. \tag{4}$$

If the solidification rate is increased from R_1 to R_2, the length of the boundary layer decreases as shown in Figure 4(b). The resulting decrease in the length of the boundary layer produces a steeper gradient in the equilibrium liquidus temperature in advance of the solidification front. This change makes it more difficult to avoid constitutional supercooling, as shown in Figure 4(c). It should be obvious that both a high thermal gradient and a low growth rate are important factors for maintaining interface stability. Therefore, a high thermal gradient to growth rate ratio (G/R) is necessary to maintain a macroscopically planar interface and, thus, to avoid constitutional supercooling in hypermonotectic samples.

The relationship presented in Eq. 3 can be used to determine the composition limits for interface stability as a function of solidification rate (assuming a fixed thermal gradient). Such a stability limit diagram was determined for the transparent analogue succinonitrile-glycerol system utilized in this study and is shown in Figure 5. The values utilized in calculating the stability limit diagram are listed in Table I. Theory indicates that a stable, macroscopically planar growth front can be maintained for compositions and solidification rates that lie below the stability limit line in this diagram.

However, even if the conditions for interface stability are met, a fibrous structure still may not be obtained during directional solidification due to problems arising from convective instability.

Table I. Definition of terms and values used in numerical calculations for the succinonitrile-glycerol system.

Symbol	Property	Value	Units	Reference
G_L	(thermal gradient in the liquid)	16.0	°C/mm	*
m_L	(slope of L_1+L_2 phase boundary)	4.6	°C/%	**
D_L	(solute diffusivity in L_2)	10^{-3}	mm^2/s	[51]
R	(growth rate)	varies	μm/s	*
C_m	(monotectic composition)	7.5%G	wt%	[21]
C_o	(alloy composition)	varies	wt%	*

* Value determined experimentally in our lab
** Value determined from partial phase diagram

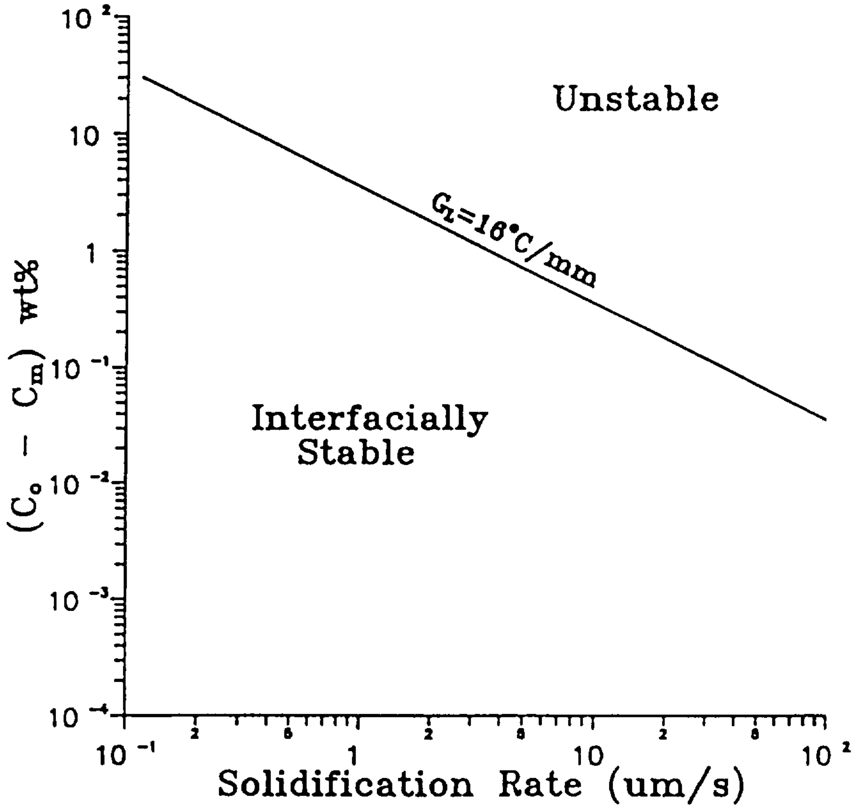

Figure 5. Stability limit diagram for the succinonitrile-glycerol system processed using a thermal gradient of 16°C/mm.

Convective Instability

As discussed above, during the directional solidification of a hypermonotectic alloy of composition C_o (see Figure 4(a)), a solute depleted boundary layer forms adjacent to the solidification front. The composition of the liquid adjacent to the solidification front is reduced to C_m, while the composition of the bulk liquid remains at C_o. Since in most known monotectic systems, the solute is the denser constituent, the solute depleted boundary layer has a lower density than the liquid above it. As a result, convective flows can occur in advance of the solidification front due to this density variation. This convective instability can apparently disrupt the solute depleted zone in immiscible alloys and, consequently, the coupled growth process.

In an effort to avoid convective instability, NASA's KC-135 aircraft has been utilized by several investigators to provide low gravity conditions during the processing of hypermonotectic samples. Fibrous composite structures have been obtained in some cases,[3,24,27-29] but there are still many questions to be answered about the reactions which occur during the morphological development of hypermonotectic composite structures. Direct observation of the reactions taking place at the growth front during solidification of hypermonotectic alloys would provide valuable insight into the mechanisms controlling solidification behavior in these potentially useful alloys. One approach used to gain a better understanding of solidification processes is to directly observe the reactions at the solidification front by using a transparent model system.

Use of Transparent Analogue Materials

The use of transparent model systems to study the solidification behavior of metals and alloys is a well-established technique. This approach has been used to study eutectic solidification,[34] to observe dendritic growth,[35-37] to model segregation in castings,[38,39] and to study growth in monotectic alloys.[21,33,40,52]

Observing solidification reactions in transparent immiscible materials has greatly increased the understanding of solidification processes. However, almost all work has been done with samples of monotectic composition. Much can still be learned by studying the solidification processes in hypermonotectic samples.

In this study, solidification events in both monotectic and hypermonotectic samples were studied using transparent immiscible samples. In order to examine morphological development in these samples during directional solidification, specialized facilities were needed. To carry out this investigation, it was necessary to design and construct a temperature gradient stage assembly.

CONSTRUCTION OF THE TEMPERATURE GRADIENT STAGE ASSEMBLY

As previously mentioned, direct observation of the reactions taking place at the growth front during directional solidification could answer many questions pertaining to solidification events in alloys of hypermonotectic composition. Observation of these reactions can be accomplished through the use of transparent analogue materials in conjunction with a temperature gradient stage (TGS) assembly attached to an optical microscope.

The temperature gradient stage assembly built for use in this study is similar in design to a directional solidification furnace. In this design, the sample is translated from a hot zone, which is held at a temperature above the melting point of the system, to a cold zone, which is held at a temperature below the melting point of the system. An exploded view of the TGS assembly showing the relative positions of the Plexiglas® cover, the hot and cold zones, the sample cell, the main body, and the microscope objective lens is presented in Figure 6

The predominant differences between a temperature gradient stage assembly and a directional solidification furnace include the specimen geometry and the optical capabilities. The cells used to contain the samples in a TGS must be made from a transparent material to allow visualization of the solidification reactions as they occur. Many other factors are important as well. For example, the design for the temperature gradient stage assembly utilized in this research had to take the following criteria into consideration:

1) The geometric limitations set by the microscope available for use.
2) The geometry of the cell used to contain the sample.
3) The thermal stability of the hot and cold zones.
4) The upper and lower temperature limits of the hot and cold zones.
5) The precision with which the sample could be positioned.
6) The range and stability of translation rates to be used.
7) The range of thermal gradients needed for experimentation.

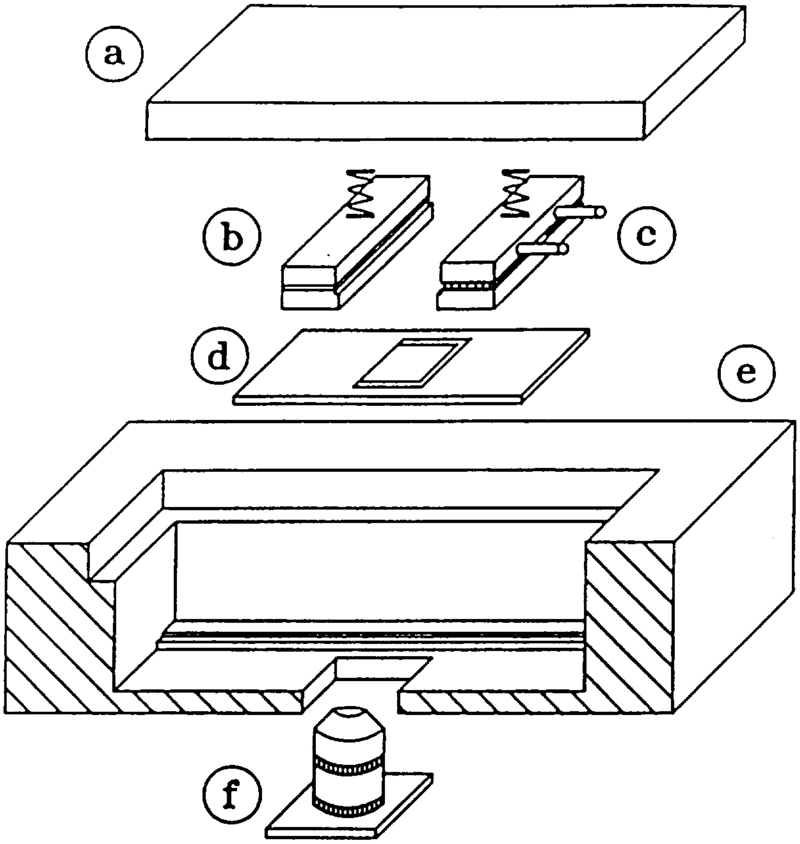

Figure 6. Exploded view of the temperature gradient stage assembly used for experimentation. Shown are (a) Plexiglas® cover, (b) hot zone, (c) cold zone, (d) sample cell, (e) main body, and (f) microscope lens.

The details involved in how these factors influenced the construction of each of the major components within the temperature gradient stage assembly will be discussed in the following sections.

Hot Zone Design

The transparent analogue system chosen for use in this study was the succinonitrile-glycerol system. The critical temperature at the top of the miscibility gap in the succinonitrile-glycerol system is 83°C. As a result, the hot zone of the TGS had to be able to exceed this temperature. A minimum upper temperature limit of 100°C was established as a design criterion to insure that a homogeneous sample could be obtained for any composition.

One of the first considerations was selection of the type of heating element to be used in the hot zone. Numerous types of heating elements were capable of maintaining a stable temperature at 100°C. Cartridge heaters and thin-film electrical resistance heaters were the two primary types of heaters considered for use in the hot zone due to their desirable geometries and due to the limitations set by the dimensions of the hot zone.

A Kapton® encapsulated, thin-film, electrical resistance heater was eventually chosen as the heating element because of its geometry, temperature capabilities, fast response time, and even heat distribution. The heater was attached to a small copper block (34 mm x 13 mm x 5 mm) which provided both the thermal mass necessary to maintain a stable hot zone temperature and a high thermal conductivity connection to the sample. The top of the thin-film heater was covered with a ceramic insulator to minimize heat loss.

A CN 2000 series temperature controller purchased from Omega Engineering was utilized to maintain a stable hot zone temperature. The controller was capable of proportional, integral, and derivative (PID) control and provided an even heating rate with little or no overshoot. A fine wire (0.13 mm) type T thermocouple was cemented into a small hole in the copper block of the hot zone to supply the necessary temperature information for the controller. A type T thermocouple was chosen for this system because it possessed the lowest standard error (±1°C) and one of the highest emf outputs per degree obtainable in the range of temperatures to be used.

The power supply for the hot zone was designed and constructed to our specifications by a local vendor. The power supply used the 4-20 milliamp output signal from the temperature controller to produce a DC voltage of 0-30 volts for the electrical resistance heater. During preliminary testing of the hot zone, it was observed that a temperature of 100°C could be easily reached within 30 seconds. This was more than sufficient for our purposes.

Cold Zone Design

In order to produce the steep thermal gradients desired in the liquid during directional solidification, a minimum temperature requirement of -25°C was selected for the cold zone of the TGS assembly. Either thermoelectric cells (TECs) or a liquid recirculating system were the two primary candidates considered to cool the copper block which would serve as the cold zone. A liquid recirculating system could provide the temperature requirements for the cold zone, but the stability and control of that temperature was uncertain. Thermoelectric cells, however, could provide thermal stability at the required operating temperature to within

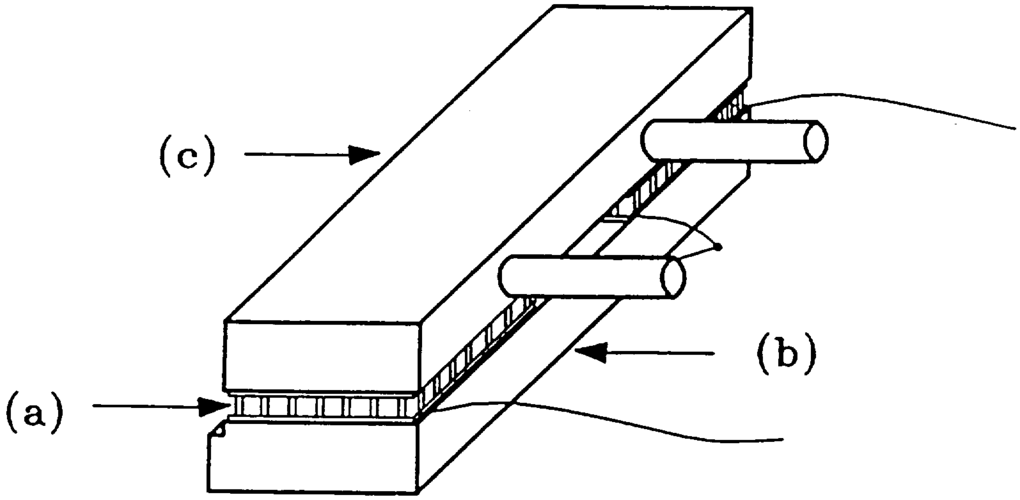

Figure 7. Schematic diagram of the cold zone constructed with (a) two thermoelectric cells placed between (b) a lower copper block which provided thermal stability for the system and (c) a heat exchanger which improved the efficiency of the system.

0.1°C. Furthermore, TECs were highly suited for this application due to their small size, wide range of operating temperatures, low power requirements, and high reliability. For these reasons, TECs were chosen for use in the construction of the cold zone. In order to maintain a stable temperature of -25°C, the cold zone was constructed using a pair of TECs connected in series electrically.

The TECs purchased for use in the cold zone were capable of establishing a maximum temperature differential of 64°C from ambient when run at full power. In order to improve the efficiency of the TECs and extend their useful life, a heat exchanger was incorporated into the cold zone design. The TECs were secured between two copper blocks using a low temperature (117°C) solder. A schematic of the assembly is shown in Figure 16. The lower copper block provided both the thermal mass necessary to maintain a stable temperature and contact with the sample cell. The upper copper block served as a heat exchanger, which was cooled by a temperature controlled fluid recirculating system. A mixture of ethylene glycol and water was used as the recirculating fluid to permit operation of the heat exchanger at temperatures below 0°C.

The TECs were controlled through the use of a SE 5000 series temperature controller and power supply purchased from Marlow Industries. The controller was capable of proportional, integral, and derivative (PID) control, and provided a ramp-to-setpoint feature. The necessary temperature information was provided to the controller by a fine wire (0.13 mm) type T thermocouple placed in the lower copper block of the cold zone.

Main Body and Other Components

The main body of the temperature gradient stage assembly was constructed from Teflon®. A deep channel was milled into the Teflon® block to provide a track for smooth translation of the sample while maintaining close lateral tolerances. Holes were drilled, where appropriate, in the main body to provide access for electrical leads, water leads, thermocouple wires, air inlets, and for mounting purposes.

Plexiglas® spacers were used to position the hot and cold zones in the main body of the temperature gradient stage assembly. The hot zone spacer was spring-loaded to allow adjustment for various spacings between the hot and cold zones. Glass spacers of various sizes were fabricated to produce numerous spacing options between the hot and cold zones, thus allowing a wide range of thermal gradients to be achieved. The position of these spacers (items c, h, and m) as well as other components is shown schematically in Figure 8.

During processing of the samples, the cold zone was operating at temperatures of -20°C and below. As a result, any moisture within the interior of the TGS assembly would result in frost formation on the cold zone. To prevent frost formation, the interior of the assembly was purged with dry air prior to lowering the cold zone temperature and a positive pressure of dry air was maintained in the interior of the temperature gradient stage throughout the sample run. To provide the necessary light path for the system while maintaining a controlled atmosphere, a Plexiglas® cover was used on the top of the assembly and a 15 mm square section of Teflon® was removed from the bottom and replaced with a thin glass plate. The light source was placed about 100 mm above

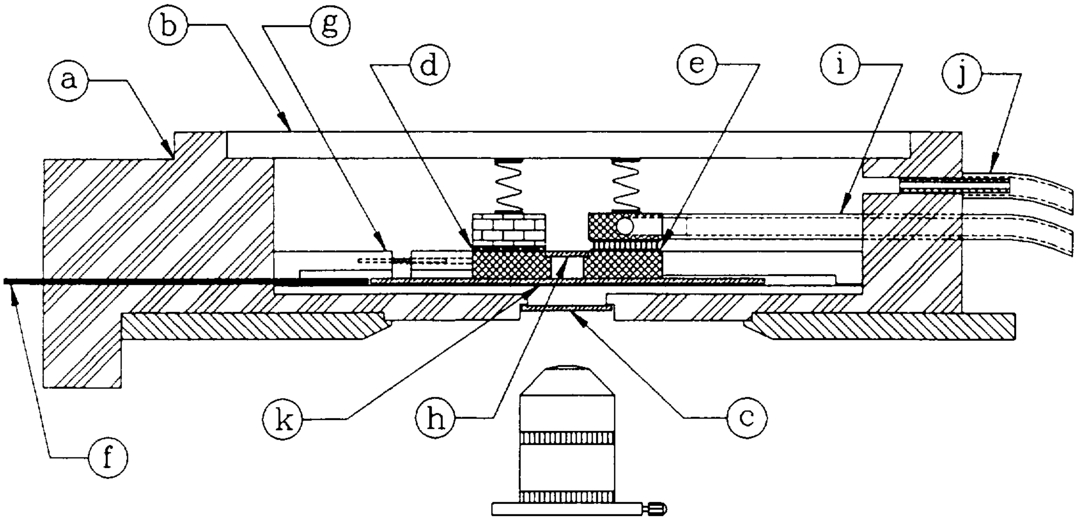

Figure 8. Cross section of the temperature gradient stage assembly showing (a) main body, (b) Plexiglas® cover, (c) hot zone spacer, (d) heater, (e) ceramic insulator, (f) heat exchanger, (g) thermoelectric cells, (h) cold zone spacer, (i) fluid recirculating line, (j) dry air inlet, (k) sample positioning rod, (l) sample cell, (m) inter-zone spacer, and (n) bottom window.

the TGS assembly and a condenser lens was used to focus the light beam on the sample. The microscope lens was positioned directly below the bottom window of the assembly. To avoid any alteration of the thermal gradient that might be caused by the light source, a heat filter was also placed in the light path above the Plexiglas® cover.

The geometry of the temperature gradient stage was such that a long working distance lens was required for the microscope. A Nikon M Plan 40x (N0015-ELWD) with a working distance of 10.1 mm and a numerical aperture of 0.5 was used with the Reichert Me F2 optical microscope.

Translation Device

The solidification rates at which morphological transitions occur in transparent systems are usually very low (0.1-5 μm/s). As a result, a translation mechanism must be utilized that will function properly at these low speeds, but still have a sufficient range of rates to permit rapid positioning of the sample when necessary. Piezoelectric micropositioning devices have a dynamic range of 6 orders of magnitude as opposed to stepping motor and gear box assemblies which, at best, have a range of 3 to 4 orders of magnitude. For these reasons, the specimen was positioned and translated using a computer controlled piezoelectric micropositioning system purchased from Burleigh Instruments, Inc., located in Fishers, New York.

The piezoelectric micropositioning system consisted of an Inchworm® motor (model number IW-710), a personal computer interface card (model 660), a joystick for manual control (model 6003), and a motor controller (model 6200). The system could translate samples at rates from 0.004 μm/s to over 2 mm/s. Precise control of the positioner was obtained through a combination of custom BASIC programs written by the user and the subroutines supplied by the manufacturer.

The translation system produced smooth linear motion with none of the backlash or leadscrew errors usually associated with screw-type drive systems. The positioner possessed a mechanical resolution (minimum step size) of 0.004 micrometers and a digital readout that displayed the position accurately to 0.5 micrometers.

An aluminum mounting bracket held the positioner in place while a stainless steel push-rod was used to move the specimen down the track beneath the hot and cold zones, thus resulting in directional solidification of the specimen.

EXPERIMENTAL PROCEDURE

Other researchers[21,32,34-40,52] have studied the solidification processes of metals with the aid of transparent analogue materials. In most cases, these materials have been contained within thin cells constructed from glass microscope slides and coverslips. A small gap is created between the glass slides by using some material as a spacer or gasket between the upper and lower slides. The interior of the cell is then filled with the transparent analogue material and processed.

It was essential that a constant, reproducible cell thickness be maintained during the processing of these materials in order to permit a valid comparison of the results between samples and to avoid any difficulties due to convective instability. To accommodate both of these requirements, the sample was contained in a thin ($< 20\ \mu m$) glass cell and placed in a horizontal orientation during processing.

Many polymeric materials were examined for potential use to provide the desired spacing between the cell walls. In addition, to prevent the immiscible liquid, L_2, from preferentially wetting the cell walls, several anti-wetting coatings were evaluated for their effectiveness during this study.

Cell Construction

The general cell geometry consisted of a standard glass microscope slide (75 mm x 25 mm x 1 mm), a U-shaped polymeric spacer, and a glass cover slip (18 mm x 18 mm x 0.15 mm) successively layered to form a cell as shown in Figure 9. After some investigation, a polyvinyl chloride spacer produced from Reynolds Plastic Wrap® was found to provide the most even and reproducible cell thickness and was implemented as the material for the polymeric spacer.

During experimentation it was observed that the immiscible L_2 phase preferentially wet the glass surfaces of the cells. This was an undesirable result, as it could presumably influence the morphology of the solidifying structure. Therefore, several anti-wetting coatings were examined in an effort to prevent the L_2 phase from wetting the cell walls. These coatings included polymerized (21) coatings of silicone oil,[53] and an evaporated carbon coating.

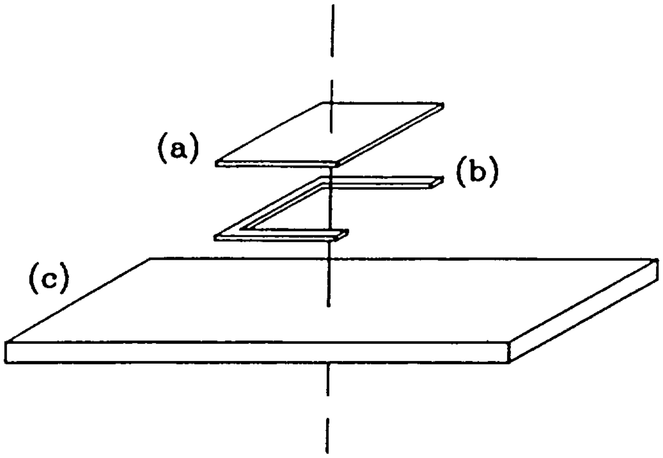

Figure 9. Schematic diagram of the general cell geometry showing relative positions of the (a) glass coverslip, (b) U-shaped polymeric spacer, and (c) glass microscope slide.

The carbon coatings proved to yield the most consistant results. In order to produce these coatings the glassware was masked with aluminum foil leaving an area approximately 14 mm square exposed. The glassware was coated with a thin layer of carbon and the cells assembled using a U-shaped polyvinyl chloride spacer. The samples processed in the carbon coated cells exhibited no visible signs of wetting and provided reproducible thicknesses.

The final cell geometry used for all samples presented in this thesis consisted of a standard glass microscope slide (75 mm x 25 mm x 1 mm), a U-shaped polyvinyl chloride (Reynolds Plastic Wrap®) spacer (12.7 μm), and a square glass cover slip (18 mm x 18 mm x 0.15 mm) successively layered to form the cell. Prior to assembly, the glassware was cleaned with ethanol and carbon coated, using a vacuum evaporator. Three edges of the coverslip were sealed to the glass slide with epoxy. The other edge was left open for the cell filling process.

Preparation of the Transparent Analogue Materials

Great care had to be taken in the preparation of these organic samples in order to avoid contamination, oxidation, and/or water absorption. A glove box with bare-hand entry ports was constructed and utilized so that a dry, oxygen-free atmosphere could be maintained during the melting and alloying steps.

The raw materials used to produce these samples consisted of 99.996% pure succinonitrile (SCN) and 99.7% pure glycerol (G). The succinonitrile was obtained from Glicksman and Koss[54] and had been distilled and zone refined to reach this purity level. The 99.7% pure glycerol was obtained from the Dow Chemical Company and was the highest purity glycerol commercially available.

The succinonitrile was stored in sealed Pyrex® tubes under a nitrogen atmosphere. In order to avoid contamination of the succinonitrile, the tubes were opened in the glove box under a nitrogen atmosphere. The succinonitrile was then melted by heating to approximately 90°C using a heat gun, and the molten succinonitrile was transferred to a 8 ml glass vial. The vial was weighed, both before and after the addition of the liquid. The weight of glycerol required to produce the desired alloy composition was calculated and then added to the vial using a disposable pipet. The vial was then capped. The next stage in sample preparation involved homogenization and cell filling.

Homogenization and Cell Filling

Homogenization of the organic alloy was carried out by heating the vial to approximately 90°C while shaking and inverting the vial until the contents were clear, indicating that only a single-phase liquid remained. The homogenized liquid was then transferred to the sample cell opening using a preheated disposable pipet. After the liquid solidified, the sample cell was quickly transferred to a vacuum filling apparatus.

The vacuum-filling apparatus was utilized to hold the sample cell during homogenization, degassing, cell filling and resolidification. The chamber was evacuated with a roughing pump and purged with nitrogen four times before final evacuation. By applying a negative DC current flow to a thermoelectric cell contained within the chamber, the sample was heated into the single-phase liquid region, allowing the constituents to melt, degas, and homogenize. The chamber was then rapidly backfilled with nitrogen to push the homogenous molten liquid into the evacuated region of the cell. Immediately after filling the cell, the sample was rapidly solidified by driving the same thermoelectric cell with a positive DC current. Next, the cell was taken out of the chamber and any excess material was cleaned from the surfaces of the glass slide and coverslip. The opening of the cell was then covered with a small (≈ 3 mm x 16 mm) rectangular strip of polyvinyl chloride and the covered opening was sealed with epoxy prior to directional solidification.

Determination of the Thermal Gradient

Some of the factors affecting the thermal gradient imposed upon the sample include the hot and cold zone temperatures, the distance separating these zones, and the thermal conductivity of the sample and its container. In this research, the operating temperatures and the distance between the zones were the only variables that could be changed to produce the desired thermal gradient with a sample.

To obtain a homogenous single-phase liquid in an immiscible system, it is necessary to operate the hot zone at a temperature well above the temperature of the L_1+L_2 phase boundary for a given composition. Furthermore, to observe all of the solidification reactions that occur in a monotectic system, it is necessary to operate the cold zone at a temperature well below that of the lowest temperature phase transformation present in the system.

To measure the thermal profile in the sample, a single 12.7 μm diameter, type K, bare-wire thermocouple was positioned in the center of the cell. The coverslip was epoxied to the glass slide on both sides and one end. The interior of the cell was filled with succinonitrile through the open end and the cell opening was then sealed with epoxy. This cell was processed under conditions identical to those used for all samples discussed herein (a hot zone temperature of 96°C, a cold zone temperature of -20°C, and a 4.6 millimeter spacing between the two zones). The thermal gradient in the sample was determined to be 15.98°C/mm.

Sample Processing Techniques

With the first samples processed, it was observed that if the samples were homogenized under the hot zone and then translated toward the cold zone, the initial stage of solidification occurred at a rapid and uncontrolled rate. This was believed to be due to a significant amount of undercooling which occurred before the onset of solidification. After the initial rapid solidification, a portion of the rapidly solidified region then remelted. This rapid solidification and remelting could lead to a change in the composition of the sample adjacent to the interface. As a result, a new approach was utilized for processing in which the leading edge of the sample was positioned under the cold zone and the remaining portion of the sample was then melted. This approach was believed to be valid for the following reason.

During sample preparation, the homogenous liquid was rapidly solidified immediately after the cell had been filled. As a result, it could be assumed that the succinonitrile and glycerol contained within the cell were uniformly distributed. If only a portion of the cell was melted, this portion should still be of the overall alloy composition and, as a result, should be representative of the entire sample. Therefore, prior to processing, the leading edge of the cell containing the sample was positioned just under the cold zone. The temperature of the cold zone was then lowered to the setpoint temperature of -20°C and allowed to stabilize. Next, the hot zone was raised to its setpoint temperature of 96°C. This resulted in melting the sample to some intermediate position between the hot and cold zones. Once the position of the solid-liquid interface stabilized and became planar, translation of the sample was started.

Using the experimental procedures discussed in this section, a matrix of directional solidification experiments was selected and these experiments were performed. These experiments utilized a wide range of growth rates and compositions. The results obtained are presented in the following section.

RESULTS AND DISCUSSION

One of the major objectives of this study was to examine solidification processes and microstructural development in off-monotectic alloys. As discussed previously, a temperature gradient stage was used in conjunction with an optical microscope to observe the directional solidification processes in transparent analogue materials contained within thin (13 μm) glass cells. During experimentation the directional solidification events were recorded with a time-lapse video cassette recorder in order to aid in analysis of the microstructural developments that occurred.

Directional solidification experiments were performed at translation rates of 0.15, 0.35, 0.70, 1.0, and 2.0 μm/s with sample compositions that included the monotectic composition (SCN-7.5wt%G) and samples 1.0 and 2.0 wt.% off of the monotectic composition (i.e. SCN-8.5wt%G and SCN-9.5wt%G, respectively). During this investigation, high thermal gradients (up to 16°C/mm) were utilized in conjunction with relatively low growth rates in an effort to avoid constitutional supercooling which would have resulted in the formation of hypermonotectic droplets in advance of the growth front and would have possibly disrupted the coupled growth process.

For the hypermonotectic samples, the effect of the solidification rate on the microstructure was examined under both conditions of a stable, macroscopically planar solidification front and under conditions of slight interfacial instability. In the samples processed under growth conditions leading to instability of the growth front, the method of incorporation of the immiscible phase into the solidifying structure was examined. The experimental results were utilized to quantitatively determine the limits of interfacial stability and the relationships between inter-fiber spacing, growth rate, and composition.

Monotectic Samples

In samples of monotectic composition, directional solidification led to the formation of a well-aligned fibrous microstructure as shown in Figure 10. The L_2 fibers that formed were of nearly uniform diameter. These fibers grew as a result of coupled growth at the solidification front and were observed for solidification velocities up to 1.0 μm/s. The L_2 fibers in these samples were relatively straight and continuous. Similar microstructures have been reported by

Figure 10. Succinonitrile-7.5 wt% glycerol sample solidified at a rate of 0.7 μm/s using a thermal gradient of 16°C/mm (G/R = 2.3×10^4°C·s/mm^2). Structure consists of well-aligned liquid fibers of the glycerol-rich phase (L_2) growing in a succinonitrile-rich solid phase (S_1) with an inter-fiber spacing of 8.7 μm and an average fiber diameter of 2.8 μm.

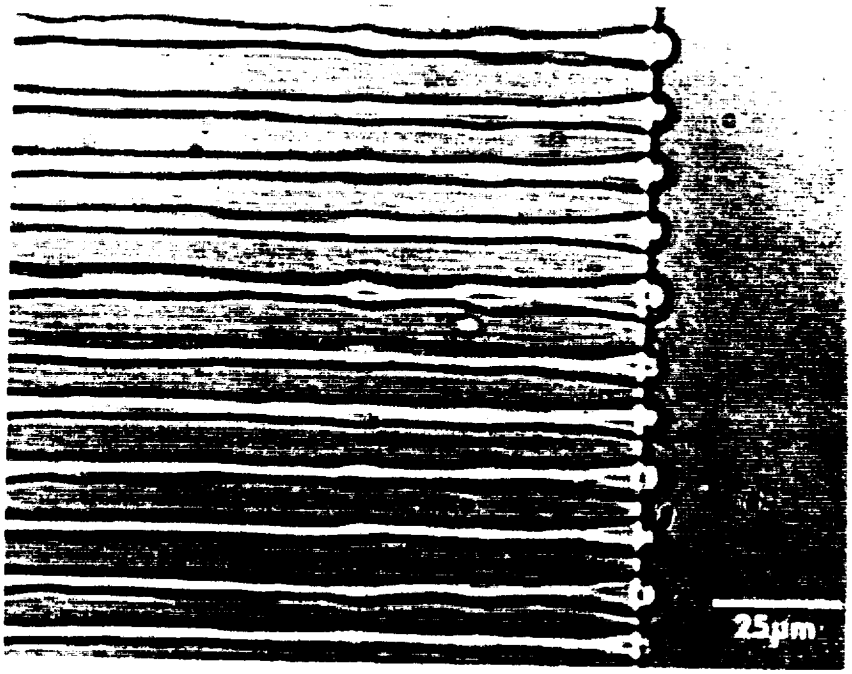
25µm

other investigators[21,33] when processing samples of monotectic composition in the succinonitrile-glycerol system.

In these monotectic composition samples, the tips (or heads) of the fibers appeared to be semicircular in shape in transmitted light microscopy. These fiber tips protruded into the liquid by a distance approximately equal to their radius (see Figure 10). In order to maintain a stable interface, both phases must grow with the same total undercooling. In monotectic systems, the interfacial energy between the two liquid phases, L_1 and L_2, will be small. As a result, the capillary undercooling in front of the L_2 will be small unless the tips of the growing liquid fibers are highly curved. Derby and Favier[32] stated that this high curvature could best be obtained through a hemispherically shaped fiber tip. This statement is consistent with the shape of the fiber tips observed in this research.

In addition, it was observed that the diameter of the L_2 fibers decreased with distance from the solidification front. At the growth front, the fiber diameter was larger by a factor of approximately two compared to the fiber diameter away from the interface. This variation can be seen in Figure 10. The diameters decreased with distance into the solid, becoming uniform at approximately 25 μm behind the growth front.

A reduction in the diameter of the L_2 fibers is actually predicted from the succinonitrile-glycerol phase diagram shown in Figure 11. As the temperature of the L_2 fibers decreased with distance from the solidification front, some solid was expected to form from the L_2 fibers. The S_1 which formed would most likely be deposited at the S_1-L_2 fiber interface. As a result, the diameter of the L_2 fibers would be reduced. The anticipated change in fiber diameter could be calculated using the phase diagram. If it is assumed that the thermal gradient in the solid near the interface was the same as that in the liquid, then the 25 μm distance over which this reduction in diameter occurred, corresponded to only a 0.4°C temperature drop. Obviously, such a dramatic change in diameter was not expected with such a small change in temperature. This phenomenon is as yet unexplained.

Another observation made for samples of monotectic composition was that the fiber diameters and inter-fiber spacings both decreased with increasing growth rate. Since the coupled growth of fibers in monotectics is a diffusion controlled process, this variation was expected. As the solidification rate of the sample increased, the time available for redistribution of solute in advance of the solidification front decreased. Since the rate of diffusion of the solute in the liquid at the solidification front was

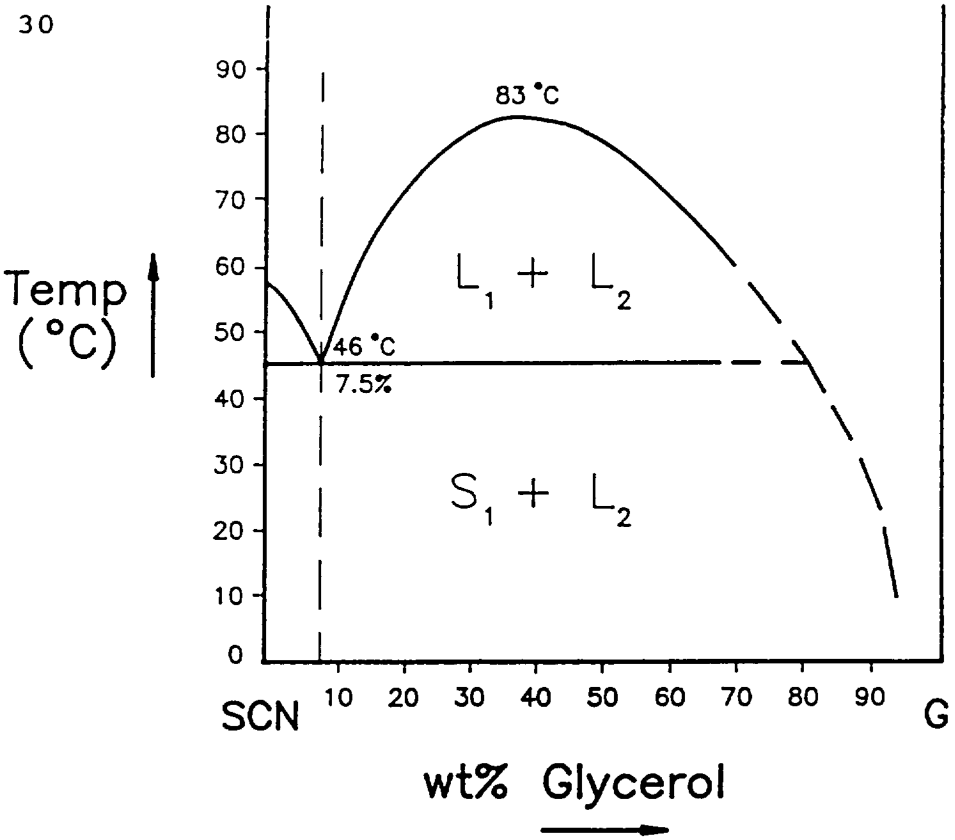

Figure 11. Partial succinonitrile-glycerol phase diagram as proposed by Kaukler.[55]

constant, the only way to accommodate the reduced time for diffusion was by reducing the distance across the growth front over which lateral solutal diffusion must occur. This meant that the fibers had to grow with a reduced inter-fiber spacing at higher solidification rates. Furthermore, if the volume fraction of fibers being incorporated into the structure was to remain the same, the fiber diameters must also decrease.

In samples of monotectic composition which were processed using growth rates higher than 1.0 μm/s, uniform, well-aligned fibrous growth was not observed. Instead, an interwoven network of fine diameter (≤ 2 μm) fibers grew in an irregular, non-parallel manner. This behavior has also been observed in SCN-7.5 wt%G samples by other investigators.[21,33] It is believed that this fine structure ripens rapidly resulting in the eventual formation of a dispersed structure.[15]

These results were all as expected, with the exception of the dramatic reduction in fiber diameter with distance into the solid. The next step in this study was to examine the directional solidification processes in hypermonotectic samples.

Hypermonotectic Samples

In an attempt to investigate interface stability and the ability to produce aligned fibrous structures in samples that were of off-monotectic composition, samples of increased glycerol content were also studied. The first hypermonotectic composition samples investigated contained 8.5 weight percent glycerol (1% off of monotectic).

From the stability limit diagram presented in Figure 5, interfacial stability was expected to occur in the SCN-8.5 wt%G samples for growth rates less than 3.5 μm/s when using a thermal gradient of 16°C/mm ($G/R = 4.6\times10^3$°C·s/mm^2). The first SCN-8.5 wt%G samples were solidified at a rate of 0.35 μm/s ($G/R = 4.6\times10^4$°C·s/mm^2), and as a result fell well within the region of stable growth predicted by Figure 5. In these samples, the formation of the hypermonotectic L_2 phase in advance of the growth front was successfully suppressed. A photomicrograph of a typical resulting structure is presented in Figure 12. To the best of our knowledge, this finding represents the first time interface stability has been demonstrated in a hypermonotectic sample of any type. The interface stability demonstrated in this sample indicates that it is possible to obtain an aligned fibrous composite structure containing a higher volume fraction of the immiscible L_2 phase than is possible in samples of monotectic composition.

The production of aligned fibrous microstructures has been reported in eutectic systems when using high G/R ratios during the processing of off-eutectic alloys.[46,48] In eutectic systems, a eutectic-like composite structure can be produced which contains a higher volume fraction of the pro-eutectic phase than is present in alloys of eutectic composition. If a stable growth front is not maintained in eutectic systems, dendrites of the primary phase can form. However, in hypermonotectic samples dendrites are not expected to form since the primary phase is a liquid. Instead, formation of droplets of the immiscible L_2 phase was expected to occur in advance of the growth front if a stable growth front was not maintained during directional solidification.

Additional SCN-8.5%G samples were processed using solidification velocities of 0.7, 1.0, and 2.0 μm/s. These higher velocities lowered the G/R ratios to 2.3×10^4, 1.6×10^4, and 0.8×10^4°C·s/mm^2. According to Figure 5, all of these G/R

Figure 12. Succinonitrile-8.5 wt%Glycerol sample directionally solidified at a rate of 0.35 μm/s using a thermal gradient of 16°C/mm (G/R = 4.6×10^4 °C·s/mm^2). Suppression of the formation of L_2 droplets in advance of the solidification front indicates that interfacial stability was obtained in this 1% off-monotectic sample.

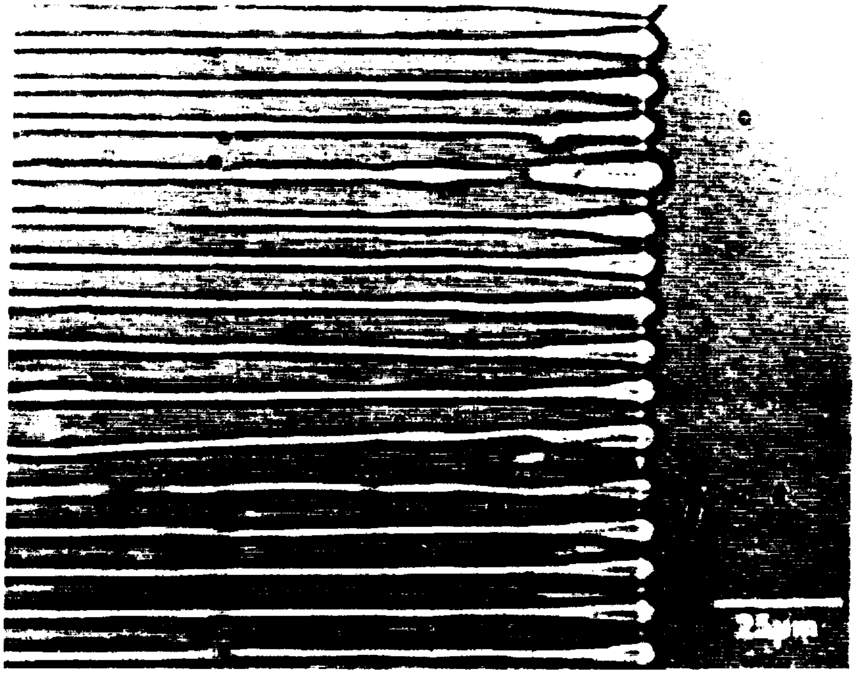
25μm

ratios should result in interfacial stability in 1% off-monotectic samples. However, when directionally solidified, all of the above samples demonstrated interfacial instability. This interfacial instability led to the formation of droplets of the L_2 phase in advance of the solidification front during processing. However, the morphologies of the resulting samples were still predominantly fibrous. The L_2 droplets did have some effect on the microstructures, depending on how the L_2 droplets were incorporated into the structure at the solidification front.

Incorporation of the L_2 droplets into the solidifying structure was observed to occur by one of two methods. A schematic diagram showing examples of both methods is included as Figure 13. In some cases, the hypermonotectic L_2 droplets came into contact with the protruding L_2 fiber tips at the solidification front and coalesced. This incorporation method had little effect on the resulting microstructure. However, other droplets were incorporated into the solid by forming a new fiber. With this incorporation method, the new fiber would eventually join with an existing fiber at the solidification front. This fiber would then remain stable as solidification continued. This sequence of events maintained a constant (inter-fiber) spacing. The method of incorporation chosen appeared to depend only upon the location at which the droplet contacted the growth front.

Suppression of the formation of the L_2 phase in advance of the solidification front (i.e. interfacial stability) in the 1% off-monotectic composition was encouraging. However, to obtain a significantly higher volume fraction of the L_2 phase in a composite structure, even higher hypermonotectic compositions were needed. As a result, the next samples processed were 2% off of monotectic composition (SCN-9.5 wt%G). These samples were used to determine if the morphologies obtained were compositionally dependent and if larger amounts of the hypermonotectic L_2 could be incorporated into the sample in fibrous form using a high G/R ratio.

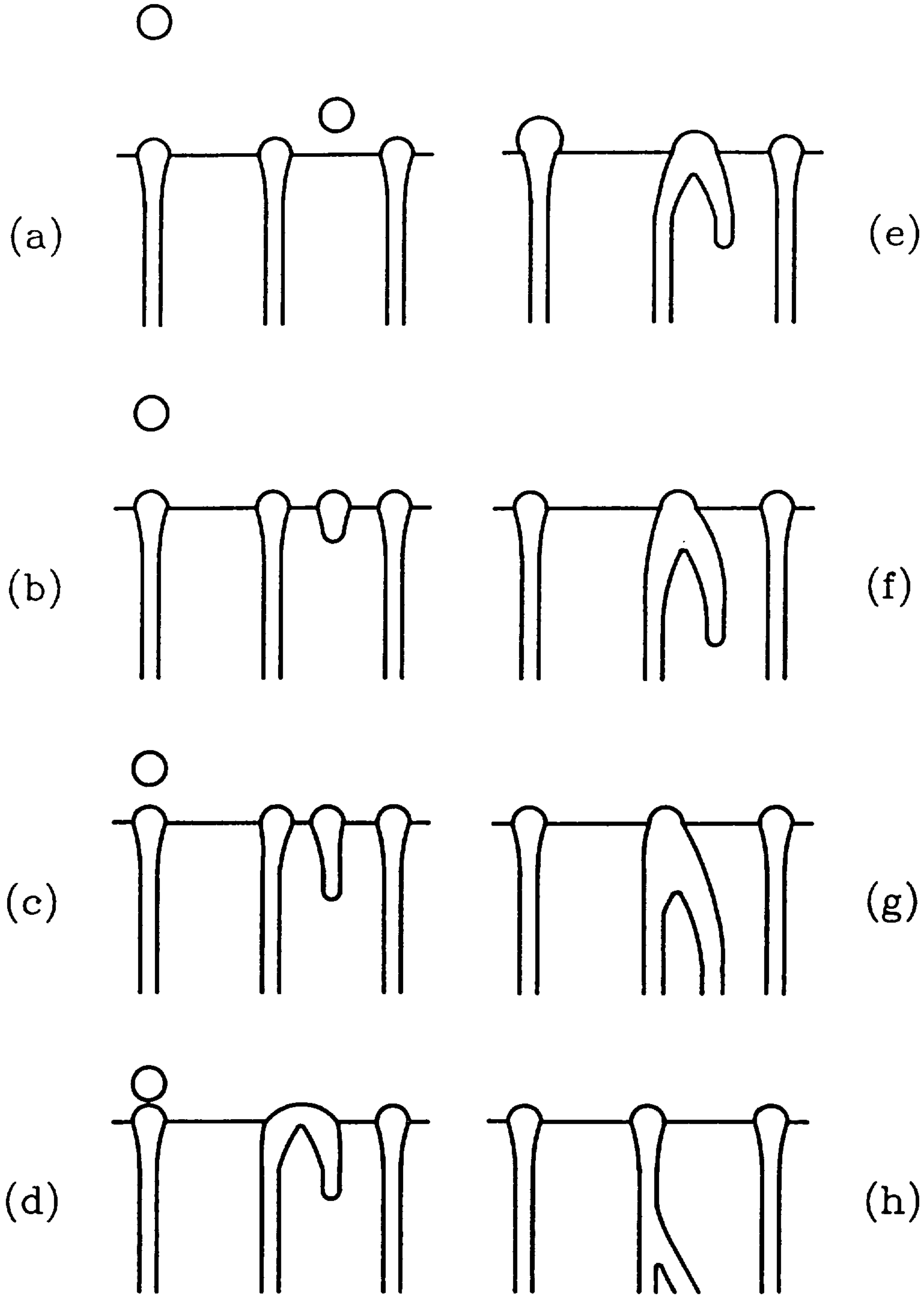

Figure 13. Schematic diagram illustrating the two methods of incorporation observed for the L_2 droplets present during growth of hypermonotectic samples under conditions of interfacial instability.

For the growth rate of 0.35 μm/s, the formation of the hypermonotectic L_2 was again suppressed in advance of the solid-liquid interface using a thermal gradient of 16°C/mm. An example of the structure formed is shown in Figure 14. This structure consisted of well-aligned fibers of L_2 with an average diameter of 3.2 μm and an inter-fiber spacing of 11.8 μm. As with both previous compositions processed under these conditions, the diameter of the rods at the growth front was seen to be approximately twice that within the solid behind the growth front.

At higher growth rates (ranging from 0.7 to 2.0 μm/s, $G/R = 2.3\times10^4$ to 0.8×10^4°C·s/mm^2), interfacial instability occurred and the excess hypermonotectic liquid was observed to nucleate in advance of the solidification front. The excess L_2 was incorporated by one of the two methods previously described.

For all growth rates utilized with the 2% off-monotectic samples, the structures obtained were very similar to those obtained in the SCN-8.5%G samples. One difference observed was a small decrease in the inter-fiber spacing. While the average diameter of the fibers obtained with all the 1% and 2% off-monotectic samples solidified at a rate of 0.35 μm/s was approximately the same (3.2 μm), the inter-fiber spacing decreased slightly from 12.1 μm to 11.8 μm between samples.

For the SCN-9.5 wt%G alloy composition only, a sample was also processed at the very low growth rate of 0.15 μm/s. In this sample, the growth front was observed to move in an oscillatory manner during solidification. The fibers which formed were semi-continuous with diameters that varied greatly (4 - 9.5 μm), as shown in Figure 15. Also, the diameters of the individual fibers varied with a periodicity that was tied to the oscillation of the growth front. Similar observations have been made by other investigators,[33] but only for samples of monotectic composition and at rates close to the structural transition (fibers → arrayed spheres) reported previously.

Figure 14. Succinonitrile-9.5 wt%Glycerol sample solidified at a rate of 0.35 μm/s with a thermal gradient of 16°C/mm ($G/R = 4.6x10^4$°C·s/mm^2). The well-aligned, continuous fibers showed an average diameter of 3.2 μm and an inter-fiber spacing of 11.8 μm.

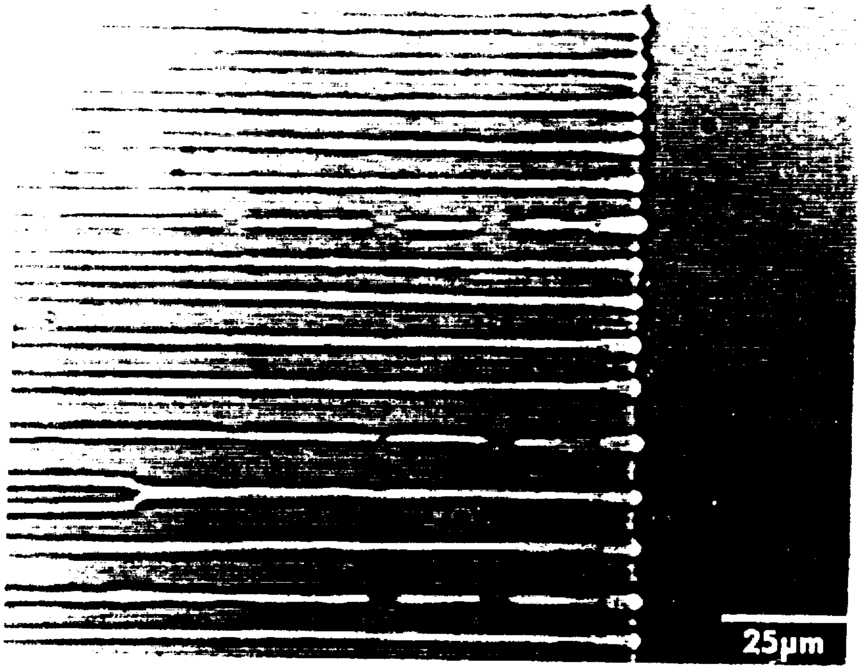
25μm

Figure 15. Photomicrograph of the SCN-9.5 wt%G sample solidified at a rate of 0.15 μm/s with a thermal gradient of 16°C/mm ($G/R = 10.7\text{x}10^{4}$°C·s/mm^{2}). The diameter of the fibers varied greatly, as did the degree of waviness.

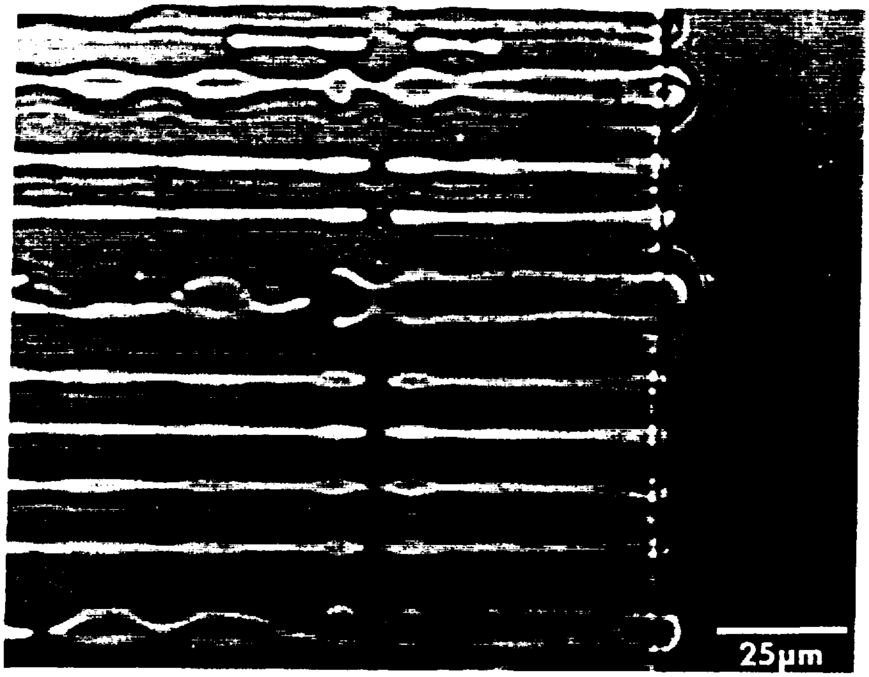
25μm

Structural Variations With Distance Solidified

One observation that was made for all of the samples studied was that fibrous composite growth only occurred for a period of time during each solidification experiment. Regardless of the composition or growth rate, the structure which formed varied somewhat along the length of the sample. In most cases, this structural variation began when one of the fibers repeatedly pinched off behind the growth front. The result was the formation of elongated globules of L_2 that were incorporated into the structure. With increasing time, a progressively larger volume fraction of the fibers began to break down in this manner until the entire structure consisted only of elongated globules. A sequence of photomicrographs illustrating the progression of this structural variation is shown in Figures 16 through 18. It should be noted that the portion of the sample over which composite growth occurred exhibited a constant inter-fiber spacing (phase spacing) with time.

One possibility for these structural variations during solidification was a compositional change along the length of the sample. This change in composition could be attributed to the initial transient expected during establishment of steady state growth, to diffusion in the liquid or to convective mixing. However, all of these effects would tend to make the interface more stable, instead of less stable, with time. As a result, these effects tend to promote fibrous growth instead of the breakdown of fibrous growth which was observed. It is more likely that the breakdown of the fibrous growth process occurred due to degradation of the organic samples with time at the temperatures used during processing.

Dependency of Inter-fiber Spacing on Growth Rate

An observation made for all the sample compositions investigated in this study was a reduction in the inter-fiber spacing with increasing growth velocities. As discussed previously, several investigators[34,42,46] have indicated a dependency of the phase or inter-fiber spacing, λ, on the growth rate, R, in eutectic systems. The predicted dependency is

$$\lambda^2 R = constant, \qquad [2]$$

where the constant is material dependent. Some investigators[19,25,32,33] have indicated that Equation 2 holds for samples of monotectic composition as well, but that the constant varies from that predicted by the equation used in the eutectic model.

Figure 16. Succinonitrile-8.5 wt%Glycerol sample forming well-aligned, continuous fibers with an average diameter of 3.2 μm and an inter-fiber spacing of 12.1 μm using a G/R ratio of 4.6x10^{4}°C·s/mm^{2} after approximately 1.8 mm of growth.

Figure 17. Photomicrograph illustrating the beginning of the breakdown of the fibrous structure shown in Figure 16 after approximately 5.0 mm of growth.

Figure 18. Photomicrograph of total structural breakdown of the SCN-8.5 wt%G sample shown in Figure 16 after approximately 6.6 mm of growth.

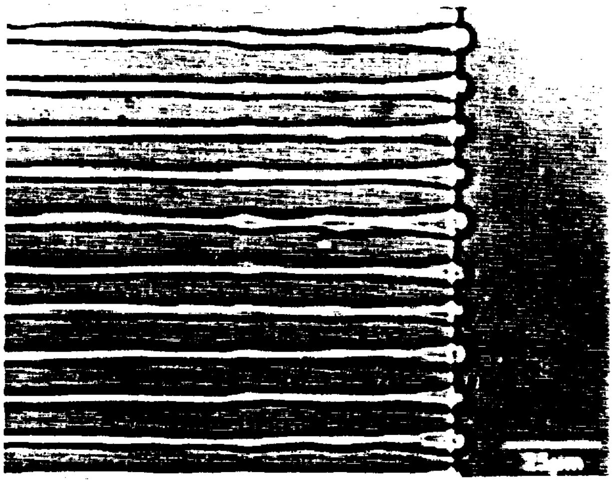
25μm

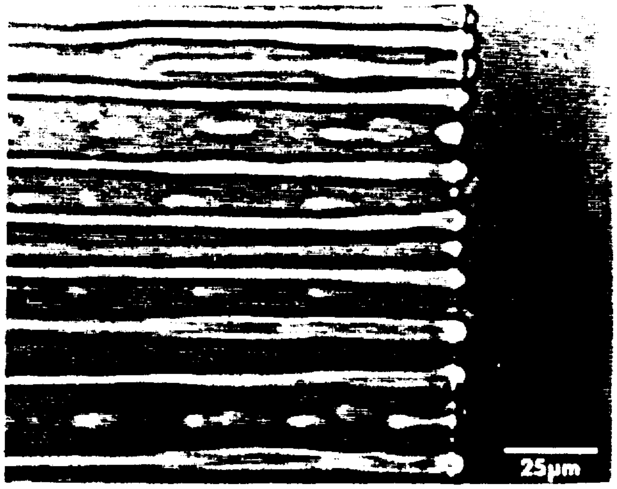
25μm

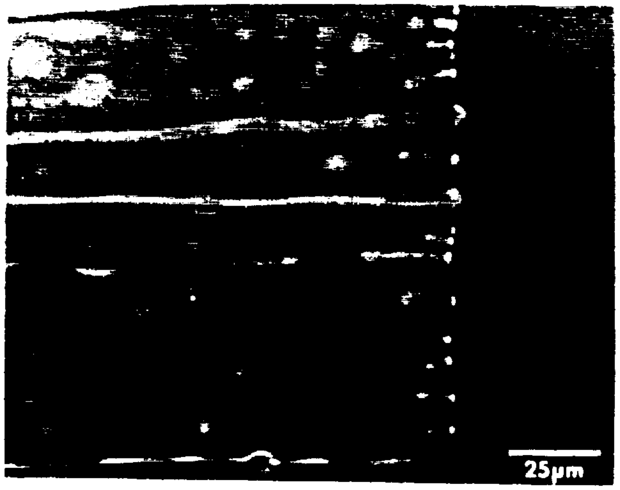
25μm

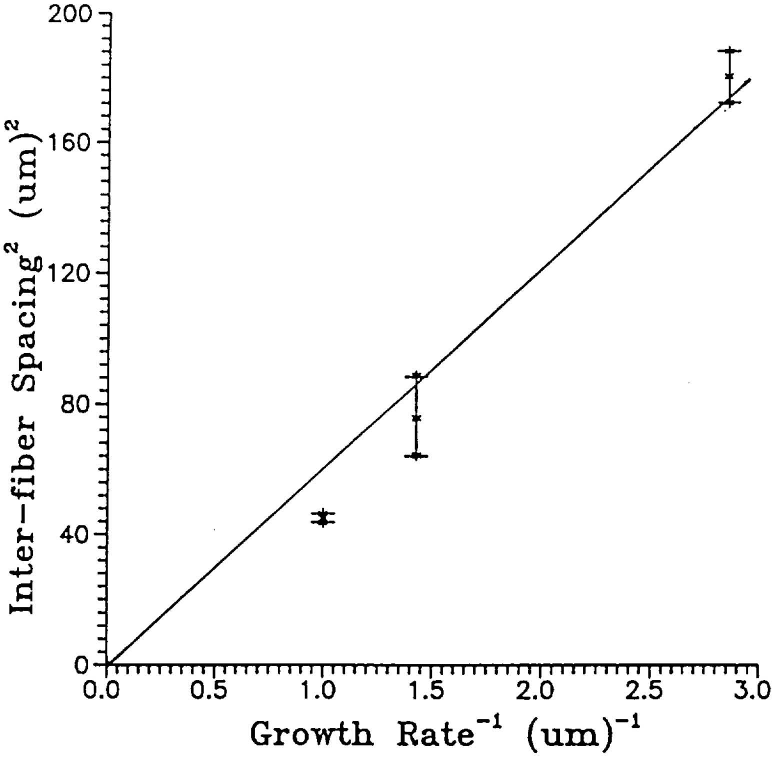

Figure 19. Plot of the square of the inter-fiber spacing versus the inverse of the growth rate for experimental data obtained using SCN-7.5 wt%G samples.

In SCN-7.5 wt%G samples, the inter-fiber spacings measured in this study were observed to decrease with increasing growth rate, as was expected. In samples solidified at 0.35, 0.70, and 1.0 μm/s, the inter-fiber spacings were measured to be 13.4, 8.9, and 6.7 μm, respectively. If the square of the phase spacing is plotted versus the inverse of the growth rate, a linear plot with a slope of "C" is expected. Data for the SCN-7.5 wt%G samples are plotted in this manner in Figure 19 and indicate that the samples obey this relationship reasonably well.

In this research, the value of the constant, C, for the λ^2R relationship was found to be equal to $0.6\text{x}10^{-16}\text{m}^3/\text{s}$ for the SCN-7.5 wt.%G samples. This value should be compared to a value of $0.4\text{x}10^{-16}\text{m}^3/\text{s}$ reported by Grugel, Lograsso, and Hellawell[33] for a SCN-7.5%G alloy. The discrepancy in these values is small and may be attributed to the differences in the thermal gradients used, as well as other factors, such as cell thickness, cell coatings, and alloy purity.

In the SCN-8.5%G samples, interfacial instability occurred at growth rates above 0.35 μm/s. However, the spacing between the fibers did not appear to be affected by the L_2 droplets forming in advance of the solidification

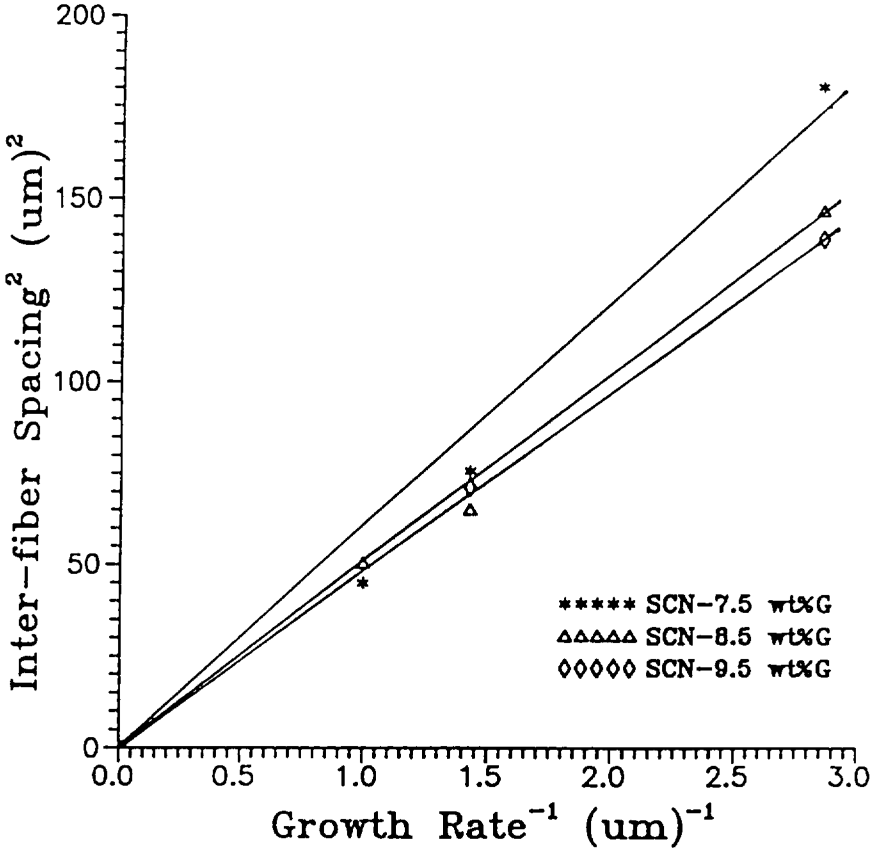

Figure 20. Plot of the square of the inter-fiber spacing versus the inverse of the growth rate for experimental data obtained using SCN-7.5 wt%G, SCN-8.5 wt%G, and SCN-9.5 wt%G samples.

front. Since the spacing did not appear to be affected, it was felt that it may be reasonable to include the data obtained in samples which exhibited slight interfacial instability in this analysis. When the square of the inter-fiber spacing was plotted versus the inverse of the growth rate for the SCN-8.5 wt%G, the data followed a linear relationship to a reasonable degree as shown in Figure 20. However, the slope of the line was observed to be slightly less than that obtained for samples of monotectic composition.

The dependency of the inter-fiber spacing on growth rate was also examined for the SCN-9.5%G samples. The sample processed at 0.15 μm/s exhibited an oscillatory growth front behavior that produced fiber diameters that varied greatly (4 - 9.5 μm). As a result, the data from this sample was not included. The elimination of this sample left quantitative data for only two growth rates, 0.35 and 1.0 μm/s, and the inter-fiber spacings were measured to be 11.8 and 8.4 μm.

The data from the SCN-9.5 wt%G samples are plotted along with those from both the monotectic and 1% off-monotectic samples in Figure 20. The results are in no way conclusive, but do indicate that a similar relationship to that seen in the SCN-7.5 wt%G samples may exist for the 1% and 2% hypermonotectic samples as well. Furthermore, with the decrease in the slope which occurs with increasing composition, it appears that the composition of the sample may affect the constant, C. This is consistent with the Jackson and Hunt[43] equation used to calculate C for eutectic systems. This equation varies inversely with the alloy composition as well as with other factors.

Quantitative Analysis of Fibrous Microstructures

Quantitative measurements were made on all samples discussed in this report. The inter-fiber spacings were determined using the line intercept method (P_L counts) performed at the growth front. The fiber diameters were measured directly from the transmitted light images. These quantitative measurements were taken both from micrographs and from a TV monitor connected to the time-lapse video cassette recorder. Measurements for the average fiber diameters were performed at points behind the growth front where the fibers had become uniform in diameter. The results for the average fiber diameters and average inter-fiber spacings are presented in Tables II and III, respectively.

The data given in Table II show that the diameters of the L_2 fibers in the monotectic and 2% off-monotectic samples decreased as the growth rate was increased. The measurable quantitative data were insufficient for an accurate analysis of the 1% off-monotectic samples. However, a decrease in diameter with growth rate was visually observed during experimentation for these samples. In addition, if the inter-fiber spacing is known, it is possible to calculate theoretical fiber diameters for these samples using the equation

$$D_f = \left[\left(\frac{4\, V_{V_f}\, H}{\pi\, k}\right)\lambda\right]^{\frac{1}{2}} . \qquad [5]$$

Table II. Average fiber diameters.

Growth Rate / Composition	0.35 μm/s	0.70 μm/s	1.0 μm/s
SCN-7.5 wt%G	3.2 ± 0.2	2.8 ± 0.1	2.3 ± 0.1
SCN-8.5 wt%G	3.2 ± 0.1	2.69*	2.52*
SCN-9.5 wt%G	3.2 ± 0.1	2.0 ± 0.1	**

* calculated values (see Appendix)
** insufficient data

Table III. Average Inter-fiber spacings.

Growth Rate / Composition	0.35 μm/s	0.70 μm/s	1.0 μm/s
SCN-7.5 wt%G	13.4 ± 0.3	8.7 ± 0.7	6.7 ± 0.1
SCN-8.5 wt%G	12.1 ± 0.8	8.0 ± 0.3	7.1 ± 0.3
SCN-9.5 wt%G	11.8 ± 0.1	8.4 ± 0.1	**

** insufficient data

The derivation of this relationship and the details of the calculations are included in the Appendix. The above results were expected and, as discussed earlier, can be explained if one considers the diffusion involved with coupled-growth processes.

The data given in Table III show that for all of the compositions examined, the inter-fiber spacing also decreased with increasing growth rate. Again, this would be expected for a diffusion-controlled, coupled-growth process.

A trend in the variation in the apparent volume fraction between samples can be determined from an analysis of the data contained in Tables II and III. The average fiber diameter is approximately 3.2 μm for all sample compositions processed at the growth rate of 0.35 μm/s, while the inter-fiber spacings decreased with increasing composition. The decrease in fiber spacing is apparent both from the data included in Table III and from the micrographs presented in Figures 21 through 23. These data indicate that more rods per unit area are being incorporated into the structure as the composition becomes increasingly hypermonotectic while the fiber diameters are remaining approximately the same for each growth rate. To the best of our knowledge, theories do not presently exist that are capable of predicting these findings.

The results obtained from this investigation have given new insight into the morphological development of hypermonotectic samples during directional solidification. It appears that high volume fraction composite materials can be produced in off-monotectic alloys under conditions of interface stability through the use of a high G/R ratio. However, models need to be developed that can explain the details of the growth processes that occur in these hypermonotectic samples.

Figure 21. Succinonitrile-7.5 wt%Glycerol sample forming well-aligned, continuous fibers with an average diameter of 3.22 μm and an inter-fiber spacing of 13.41 μm (G/R = 4.6×10^{4} °C·s/mm^2).

Figure 22. Succinonitrile-8.5 wt%Glycerol sample forming well-aligned, continuous fibers with an average diameter of 3.21 μm and an inter-fiber spacing of 12.09 μm (G/R = 4.6×10^{4} °C·s/mm^2).

Figure 23. Succinonitrile-9.5 wt%Glycerol sample forming well-aligned, continuous fibers with an average diameter of 3.16 μm and an inter-fiber spacing of 11.76 μm (G/R = 4.6×10^{4} °C·s/mm^2).

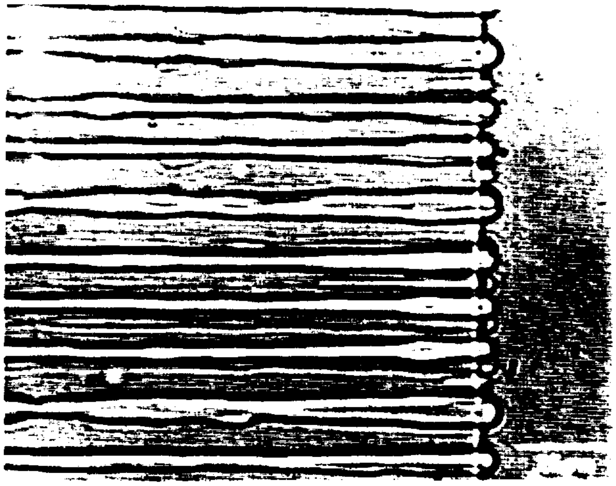

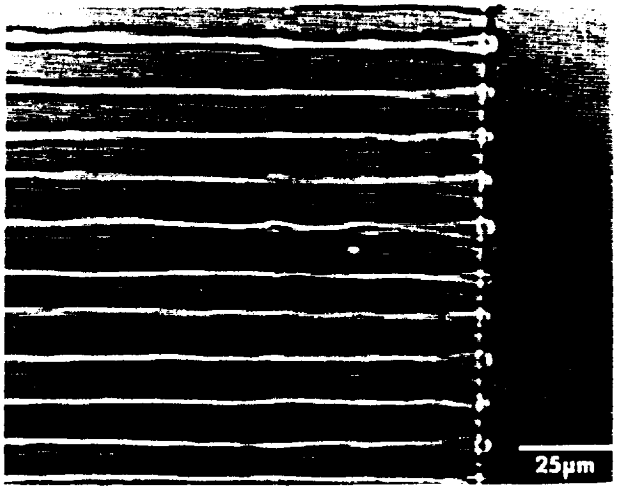
25µm

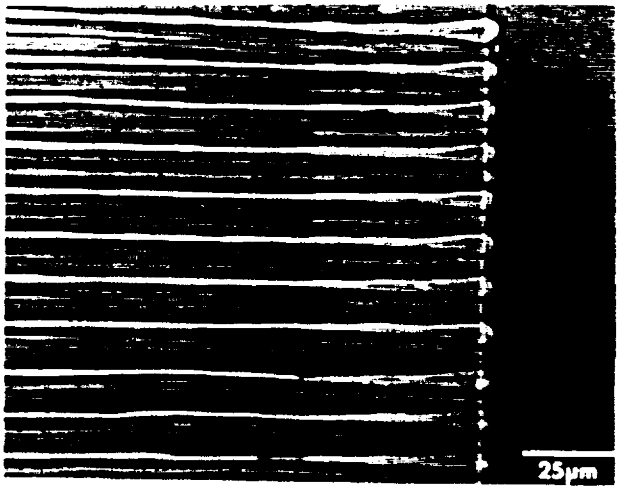
25µm

CONCLUSIONS

This investigation was focused on the visual examination of solidification processes and microstructural development of the transparent analogue system succinonitrile-glycerol. Both monotectic and off-monotectic compositions were examined over a range of growth rates to determine if interfacial stability could be maintained in samples of hypermonotectic composition during directional solidification through the use of high thermal gradient to growth rate ratios (G/R).

Based on the results obtained from this investigation, the following conclusions can be made:

(1) Interfacial stability, leading to the production of fibrous microstructures, can be maintained under conditions of steady state growth for alloys up to 2% off of monotectic composition by using a high thermal gradient to growth rate ratio (4.6×10^4 °C·s/mm^2 or greater).

(2) For the sample geometry utilized, as the alloy composition is increased, the volume fraction of fibers produced in the microstructure is increased by decreasing the inter-fiber spacing while the diameters of the fibers remain approximately constant for a given growth rate.

(3) For both monotectic and hypermonotectic alloys, a linear relationship exists between the square of the inter-fiber spacing and the inverse of the growth rate. For various alloy compositions, the slope of the linear relationship varies inversely with composition.

(4) In samples processed under conditions of slight interfacial instability, the method of incorporation of the excess hypermonotectic liquid droplets does not lead to breakdown of the formation of a fibrous microstructure.

REFERENCES

1. J. L. Reger: *Interim Report*, Contract NAS8-28267 NASA Marshall Space Flight Center, TRW System Group, Redondo Beach, CA, May 1973.

2. A. Kamio et al.: *Trans. Jpn. Inst. Met.*, 1984, vol. 25, pp. 569-74.

3. A. C. Sandlin: *Ph.D. dissertation*, University of Alabama at Birmingham, 1989.

4. A. Bergman et al.: *Materials Processing in the Reduced Gravity Environment of Space*, Elsevier Science Publishing Co., New York, NY, 1982, pp. 579-91.

5. R. N. Grugel and R. Poorman: *Materials Science Forum*, 1989, vol. 50, pp. 89-100.

6. L. L. Lacy and C. Y. Ang: *Apollo-Soyuz Test Project*, NASA Johnson Space Center, 1977, vol. I, pp. 403-28.

7. S. H. Gelles and A. J. Markworth: *AIAA J.*, 1978, vol. 16(5), pp. 431-8.

8. S. H. Gelles and A. J. Markworth: *IV-1.SPAR V Final Report*, NASA Experiment No. 74-30.

9. J. B. Andrews, A. C. Sandlin, and P. A. Curreri: *Metall. Trans., A,* 1988, vol. 19A, pp. 2645-50.

10. A. Deruyterre and L. Froyen: *Proceedings of the Workshop on Effect of Gravity on Solidification of Immiscible Alloys*, Stockholm, ESA SP-219, 1984, pp. 65-7.

11. L. Ratke, W. K. Thieringer, and H. Fischmeister: *Proceedings of the Norderney Symposium on Scientific Results of the German Spacelab Mission D1*, Norderney, Germany, 1986, pp. 332-41.

12. J. B. Andrews, C. J. Briggs, and M. B. Robinson: *Proceedings of the VIIth European Symposium in Materials and Fluid Sciences in Microgravity*, Oxford, UK, ESA SP-295, 1990, pp. 127-33.

13. C. Potard: *Materials Processing in the Reduced Gravity Environment of Space*, Elsevier Science Publishing Co., Inc., New York, NY, 1982, pp. 543-51.

14. C. Potard: *Proceedings of the Workshop on Effect of Gravity on Solidification of Immiscible Alloys*, Stockholm, ESA SP-219, 1984, pp. 79-82.

15. F. Toloui, A. J. Macleod, and D. Double: *In Situ Composites IV*, Elsevier Science Publishing Co., New York, NY, 1982, pp. 253-66.

16. R. Grugel and A. Hellawell: *Metall. Trans., A,* 1981, vol. 12A, pp. 669-81.

17. R. Grugel, T. Lograsso, and A. Hellawell: *Materials Processing in the Reduced Gravity Environment of Space*, Elsevier Science Publishing Co., New York, NY, 1982, pp. 553-61.

18. A. C. Sandlin: *Master's thesis*, University of Alabama at Birmingham, 1986.

19. G. A. Chadwick: *Br. J. Appl. Phys.*, 1965, vol. 16, pp. 1095-7.

20. M. H. Johnston and R. A. Parr: *Proceedings of the Conference on In-Situ Composites-III*, Ginn Custom Publishing, Boston, MS, 1978, pp. 49-58.

21. R. N. Grugel and A. Hellawell: *Metall. Trans., A*, 1984, vol. 15A, pp. 1626-31.

22. J. B. Andrews et. al: *Proceedings for the AIAA/IKI Microgravity Science Symposium*, Moscow, USSR, 1991, pp. 238-46.

23. J. B. Andrews, A. C. Sandlin, and R. A. Merrick: *Advances in Space Research*, 1991, vol. 11(7), pp. (7)291-5.

24. J. B. Andrews, A. L. Schmale, and, A. C. Sandlin: *J. Cryst. Growth*, In Press.

25. J. D. Livingston and H. E. Cline: *Trans. TMS-AIME*, 1969, vol. 245, pp. 351-7.

26. Z. B. Dwyer and J. B. Andrews: *Proceedings of 4th International Symposium in Experimental Methods for Microgravity Materials Science Research III*, San Diego, CA, 1992, In Press.

27. A. C. Sandlin, J. B. Andrews, and P. A. Curreri: *Proceedings of the VIIth European Symposium in Materials and Fluid Sciences in Microgravity*, 1991, vol. 77, pp. 127-33.

28. J. B. Andrews et. al: *Materials Science Forum*, 1991, vol. 77, pp. 269-81.

29. A. C. Sandlin, J. B. Andrews, and P. A. Curreri: *Metall. Trans., A*, 1988, vol. 19A, pp. 2665-9.

30. S. Shah, R. N. Grugel, and B. D. Lichter: *Metall. Trans., A*, 1988, vol. 19A, pp. 2677-80.

31. J. W. Cahn: *Metall. Trans., A*, 1979, vol. 10A, pp. 119-21.

32. B. Derby and J. J. Favier: *Acta Metall.*, 1983, vol. 31(7), pp. 1123-30.

33. R. N. Grugel, T. A. Lograsso, and A. Hellawell: *Metall. Trans., A*, 1984, vol. 15A, pp. 1003-12.

34. J. D. Hunt and K. A. Jackson: *Trans. TMS-AIME*, 1966, vol. 236, pp. 843-52.

35. A. Papapetrou: *Z. Kristallogr.*, 1935, vol. 92(A), p. 89.

36. K. A. Jackson and J. D. Hunt: *Acta Metall.*, 1965, vol. 13, p. 1212.

37. K. A. Jackson, J. D. Hunt, D. R. Uhlmann and T. P. Steward, III: *Trans. TMS-AIME*, 1966, vol. 236, p. 149.

38. R. J. McDonald and J. D. Hunt: *Trans. TMS-AIME*, 1969, vol. 245, p. 1933.

39. S. M. Copley, A. F. Giamei, S. M. Johnson and M. F. Hornbecker: *Metall. Trans., A*, 1970, vol. 1A, p. 2193.

40. H. Song and A. Hellawell: *Metall. Trans., A*, 1989, vol. 20A, pp. 171-7.

41. R. A. Merrick and J. B. Andrews: TMS Annual Meeting, Anaheim, CA, February, 1991.

42. K. A. Jackson and J. D. Hunt: *Trans. TMS-AIME*, 1966, vol. 236, pp. 1129-42.

43. R. N. Grugel: Vanderbuilt University, private communication, 1992.

44. Z. B. Dwyer and J. B. Andrews: University of Alabama at Birmingham, Birmingham, AL, private communication, 1992.

45. Y. Kamotani, S. Ostrach, and S. Lowry: *Materials Processing in the Reduced Gravity Environment of Space*,

Elsevier Science Publishing Co., New York, NY, 1982, pp. 161-72.

46. F. R. Mollard and M. C. Flemings: *Trans. TMS-AIME*, 1967, vol. 239, pp. 1534-46.

47. D. Beysens: *Proceedings from Workshop on Systems with a Liquid Miscibility Gap*, Bad Honnef, Germany, May 1992, In Press.

48. J. B. Verhoeven, K. K. Kingery, and R. Hofer: *Metall. Trans., B*, 1975, vol. 6B, pp. 647-52.

49. M. C. Flemings: *Solidification Processing*, McGraw-Hill, Inc., New York, NY, 1974, pp. 107-12.

50. W. A. Tiller: *ASM*, 1958, pp. 276-318.

51. R. J. Schaefer and S. R. Coriell: *Metall. Trans., A,* 1984, vol. 15A, pp. 2109-15.

52. W. F. Kaukler and D. O. Frazier: *Nature*, 1986, vol. 323, pp. 50-2.

53. D. O. Frazier: NASA Marshall Space Flight Center, Huntsville, AL, private communication, February 1990.

54. M. Glicksman and M. Koss: Rensselaer Polytechnic Institute, Materials Engineering Department, Troy, NY.

55. W. F. Kaukler: NASA Marshall Space Flight Center, Huntsville, AL, private communication, January 1990.

APPENDIX

Derivation of the Equation for the Fiber Diameter as a Function of the Inter-fiber Spacing

In some of the samples processed, the image quality was poor and accurate quantitative data could not be obtained to determine the average fiber diameter within the microstructure. However, data were obtainable for the inter-fiber spacing. The following mathematical approach was used to calculate the expected diameters from these samples.

The total volume, V_f, occupied by all the fibers within a cell is

$$V_f = A_f * N * L, \qquad [A1]$$

where A_f = area of the fiber
N = number of fibers, and
L = length of the fibers.

It follows that the volume fraction of fibers, V_{V_f}, is equal to the volume of all the fibers divided by the total volume of the cell or

$$V_{V_f} = \frac{V_f}{V_{cell}} = \frac{A_f * N * L}{L * W * H}, \qquad [A2]$$

where L = length of the cell
W = width of the cell, and
H = height of the cell.

Assuming that the fibers are approximately cylindrical in shape, the area of a fiber, A_f, would be that of a circle multiplied by a shape factor, k, to correct for any imperfection in shape, or

$$A_f = \left(\frac{\pi D_f^2}{4}\right) k, \qquad [A3]$$

whereD_f = diameter of the fiber.

Substituting Eq. A3 into Eq. A2 and cancelling like terms yields

$$V_{V_f} = \frac{(\frac{\pi D_f^2}{4})\ k * N}{W * H}. \qquad [A4]$$

The width of the cell can be given by the equation

$$W = (D_f\ N) + (\lambda - D_f)\ N,$$

which reduces to

$$W = \lambda * N, \qquad [A5]$$

where λ = inter-fiber spacing (center to center). Substituting Eq. A5 into Eq. A4 and cancelling like terms yields

$$V_{V_f} = \frac{(\frac{\pi\ D_f^2}{4})\ k}{\lambda * H}. \qquad [A6]$$

Solving Eq. A6 for D_f^2 yields

$$D_f^2 = (\frac{4\ V_{V_f}\ H}{\pi\ k})\ \lambda,$$

where

$$(\frac{4\ V_{V_f}\ H}{\pi\ k}) = constant. \qquad [A7]$$

Thus, Eq. A6 reduces to

$$D_f^2 = \lambda\ A, \qquad [A8]$$

where A is equal to the constant in Eq. A7.

To verify Eq. A7 and determine the experimental value for A, data for the average fiber diameters and inter-fiber spacings from the SCN-7.5 wt%G samples were plotted and are shown in Figure A1.

These data appear to obey a reasonably linear relationship with a slope, A, of 0.802.

For the SCN-7.5 wt%G samples, the constant from Eq. A7 was found to be

$$\frac{4\ V_{V_f}\ H}{\pi\ k} = 0.802$$

or

$$k = \frac{4\ V_{V_f}\ H}{0.802\ \pi}\ . \qquad [A9]$$

For the SCN-7.5 wt%G alloy, V_v was calculated to be 8.02%. The cell spacing, H, used in this study was 13 μm.

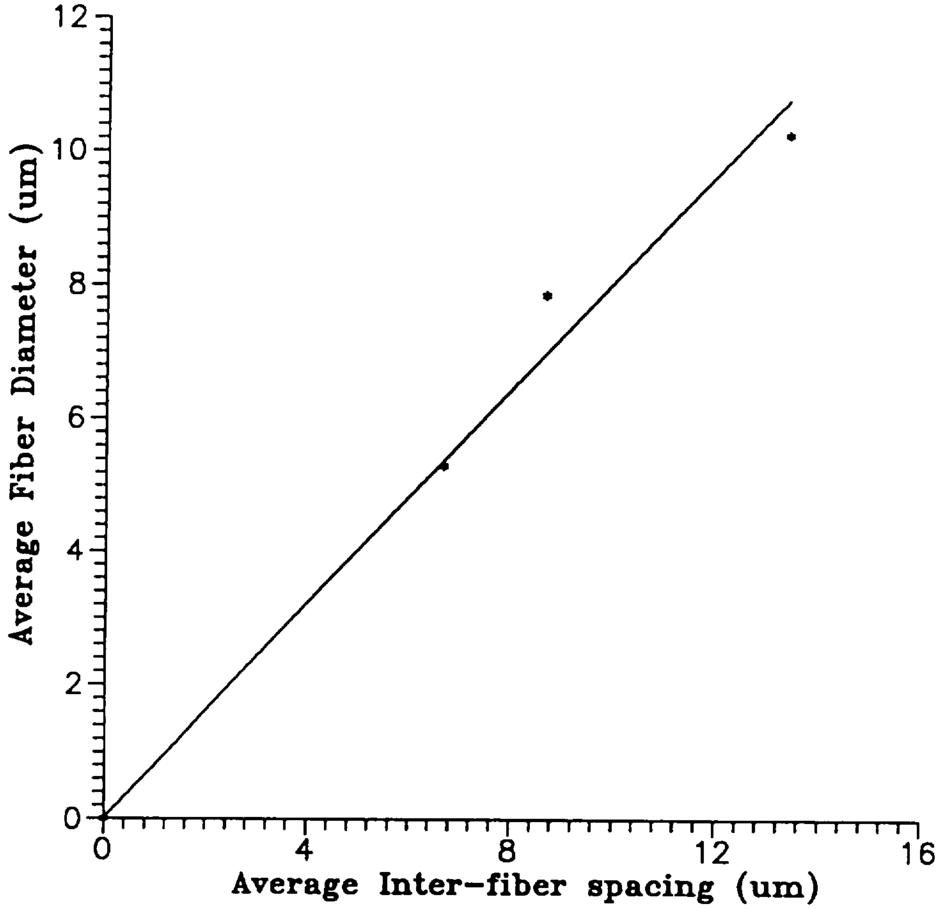

Figure A1. Plot of the square of the fiber diameter versus the inter-fiber spacing for the SCN-7.5 wt%G samples processed at 0.35, 0.7, and 1.0 μm/s.

Substituting these values into Eq. A9 yields

$$k = \frac{4(0.0802)(13)}{0.802\ \pi} = 1.6552.$$

The V_v for the SCN-8.5 wt%G alloy was calculated to be 8.99%. Thus, substituting this value into Eq. C7 to determine a theoretical constant for the SCN-8.5 wt%G alloy yields

$$C_{8.5\%} = \frac{4(0.0899)(13)}{(1.6552)\ \pi} = 0.899.$$

Using this theoretical constant for the 8.5%G samples and Eq. A8 yields

$$D_f^2 = 0.899(\lambda)$$

or

$$D_f = [(0.899)\lambda]^{\frac{1}{2}}. \qquad [A10]$$

Eq. A10 was used to determine the fiber diameters shown in Table II.